Minimally Invasive Characterization and Real-Time Simulation of Viscoelastic Soft Tissue Behavior

by

Evren Samur

A Thesis Submitted to the
Graduate School of Engineering
in Partial Fulfillment of the Requirements for
the Degree of

Master of Science

in

Mechanical Engineering

Koç University

October 2005

Koç University

Graduate School of Sciences and Engineering

This is to certify that I have examined this copy of a master's thesis by

Evren Samur

and have found that it is complete and satisfactory in all respects,
and that any and all revisions required by the final
examining committee has been made.

Committee Members:

Çağatay Başdoğan, Ph. D. (Advisor)

Burak Erman, Ph. D.

Murat Sözer, Ph. D.

Date: Oct 03, 2005

ABSTRACT

The lack of experimental data in current literature on material properties of live soft tissues has been a significant impediment in the development of realistic soft tissue models for virtual reality based surgical simulators used for medical training. This thesis presents an inverse finite element solution for soft tissue characterization based on experimental data and a new numerical scheme for real-time simulation of viscoelastic soft tissue behavior. A robotic indenter was developed for minimally invasive measurement of tissue properties during a laparoscopic surgery. Using the indenter, animal experiments were conducted in-situ and force-displacement and force-time responses of pig liver under static and dynamic loading conditions were successfully measured to characterize its elastic and time-dependent material properties. An effective elastic modulus of the liver was estimated as 10-15 kPa from the force-displacement data of static indentations based on the small deformation assumption. Then, using the same assumption, the stress relaxation function, describing the variation of stress with respect to time, was determined from the force-time data through curve fitting. Finally, an inverse finite element solution was developed using ANSYS finite element package to calculate the optimum values of viscoelastic and nonlinear hyperelastic material properties of pig liver. The initial values and the constraints of the optimization were determined from the effective elastic modulus and the stress relaxation function. The optimized material parameters were then integrated into a 3D finite element model for real-time simulation of a viscoelastic soft tissue behavior. A new numerical scheme and a pre-computation approach were developed for real-time computation and display of nodal displacements and interaction forces. The developed finite element model and the proposed pre-computation approach were both validated using ANSYS.

ACKNOWLEDGEMENTS

I would like to express my sincere gratitude and appreciation to my advisor, Assist. Prof. Dr. Çağatay Başdoğan for his expert guidance, suggestions and constructive criticisms at all phases of this study. I am grateful to Assist. Prof. Dr. Çağatay Başdoğan also for his generous and continuous support in other phases of my life.

I would like to thank to Mert Sedef for his kindness, sharing his knowledge and sparing his time whenever I need help.

I would like to thank to Assoc. Prof. Dr. Levent Avtan and Assist. Prof. Dr. Oktay Düzgün for their cooperation to perform animal experiments.

I am very grateful to my family and special friends for their love and support.

TABLE OF CONTENTS

LIST OF TABLES

LIST OF FIGURES

NOMENCLATURE

σ	stress
ε	strain
ε_S	strain in a spring
σ_S	stress in a spring
ε_D	strain in a dashpot
σ_D	stress in a dashpot
$\boldsymbol{\sigma}$	Cauchy stress tensor
$\boldsymbol{\varepsilon}$	strain tensor
τ	relaxation time
$\Delta\varepsilon$	infinitesimal strain increment
$\Delta\sigma$	infinitesimal stress increment
s	arbitrary time between 0 and t
E	effective elastic modulus
E(t)	elastic relaxation function
G	effective shear modulus
G(t)	shear stress relaxation function
E_j	independent stiffness parameter
E_∞	long-term (final) elastic modulus
E_0	short-term (initial) elastic modulus
G_∞	long-term (final) shear modulus
G_0	short-term (initial) elastic modulus

N	number of the Maxwell elements
$\boldsymbol{X}$	material (Lagrangian) coordinates
$\boldsymbol{x}$	spatial (Eulerian) coordinates
$\boldsymbol{F}$	deformation gradient tensor
v	deformed volume
V	undeformed volume
J	jacobian of transformation
u	displacement field
$\boldsymbol{C}$	right Cauchy-Green deformation tensor
I_1, I_2, I_3	principle invariants
$\boldsymbol{E}$	Lagrangian Green's strain tensor
$\boldsymbol{T}$	first Piola-Kirchhoff stress tensor
$\boldsymbol{S}$	second Piola-Kirchhoff stress tensor
W	strain-energy function
$C_{ij}, \mu_i,$	nonlinear material stiffness constants
C_{10}, C_{01}	coefficients of Mooney-Rivlin strain-energy function
λ	principle stretch ratio
SP	set point
PV	process variable
CV	control variable
K_P, K_D, K_I	proportional, derivative, and integral gains
δ	indentation depth
P	force
R	radius of a rigid sphere
ν	Poisson ratio
G_k, τ_k	coefficients of relaxation function
FKN	contact stiffness factor
FTOLN	penetration tolerance factor
α_j	relative modulus
DVs	design variables
SVs	state variables
F_j^{EXP}	experimental force value of j^{th} data point

F_j^{FEM}	force value of j^{th} data point obtained from FEM simulation
Δt	time step
t_{n+1}	current time step
h	internal stress variable
$\boldsymbol{h}$	internal stress variable in tensor form
γ_j	normalized coefficients of relaxation function
σ_0	initial stress
$\boldsymbol{\sigma_0}$	initial stress in tensor form
$\boldsymbol{\Omega}$	object model
${}_eN_i\ (\boldsymbol{x})$	basis functions
$\boldsymbol{u(x)}$	displacement field
Π_{ext}	work done by external forces
${}_eV$	volume of an element
Π	total potential energy
${}_e\boldsymbol{u}$	displacement of an element
$\boldsymbol{C_{elastic}}$	material stiffness matrix
$\boldsymbol{B}$	constant matrix
μ, λ	Lamé constants
${}_e\boldsymbol{f}$	discretized force vector for an element
$\boldsymbol{K_T}$	constant tangent stiffness matrix
$\boldsymbol{U}^n$	vector of nodal displacements at previous time step n
$\boldsymbol{K_{hist}}$	history stiffness matrix
$\boldsymbol{H}^{n+1}$	history matrix at current time step $n+1$
N_e	number of elements
$\boldsymbol{F_{hist}}$	internal load history vector
$\boldsymbol{F_{ext}}$	external load vector
${}_e\boldsymbol{U}^n$	nodal element displacements for the current time step n

Chapter 1

INTRODUCTION

The lack of data in current literature on *in-vivo* and *in-situ* material properties of soft tissues has been a significant obstacle in the development of virtual reality based surgical simulators that can provide the user with realistic visual and haptic feedback for training medical personnel [1]. Most tissue experiments conducted in the past were *in-vitro* studies and were performed in controlled laboratory conditions. The experimental data has been collected under well-defined boundary conditions from tissue samples of known geometries [8]. However, recent experimental studies report that tissue properties obtained through *in-vitro*, *ex-vivo*, and *in-vivo* measurements show significant differences in material properties [9, 10, 11]. Considering the fact that integration of incorrect material properties into deformable tissue models for surgical simulation may cause adverse training effects, it is obvious that acquiring *in-vivo* and *in-situ* tissue properties is an important research problem which is addressed in this thesis. Soft organ tissues exhibit complex nonlinear, anisotropic, nonhomogeneous, time, and rate dependent behavior, which are extremely challenging to measure and simulate.

In this thesis, we present new approaches for minimally invasive measurement and real-time simulation of soft tissue behavior. We developed a robotic indenter to measure *in-vivo* material properties of soft tissues. In comparison to the other measurement systems referred in the literature, our robotic measurement system is minimally invasive and designed to make controlled indentations on internal organs in abdominal region during a laparoscopic surgery. Three different sets of animal experiments were conducted in an operating room to obtain force-displacement and force-time curves of pig liver under static and dynamic loading conditions for characterization of viscoelastic and nonlinear hyperelastic material properties. An inverse finite element solution was developed using ANSYS finite element package to calculate the material properties through iterations. We then

integrated the estimated material properties into a 3D finite element model for realistic simulation of soft tissue behavior. A new numerical scheme and a pre-computation approach were developed for real-time computation and display of nodal displacements and interaction forces. While the superposition approach has been applied to real-time static FEM simulation in the past [3, 46], to our knowledge, it has not been extended to real-time linear viscoelastic simulation yet.

The following chapter provides necessary background and literature review related to the characterization and simulation of soft tissue behavior. The minimally invasive surgery, soft tissue measurement techniques and simulation methods are also reviewed. Chapter 3 gives the fundamentals of solid mechanics. An introduction to linear viscoelasticity and nonlinear continuum mechanics are presented. Design details of our robotic indenter are given in Chapter 4. In addition, the controller design and the preliminary experiments are presented. Experimental setup and procedures are described in Chapter 5. Types of stimuli and the results of the animal experiments are also given in this chapter. Chapter 6 presents the estimated material properties of pig liver based on the experimental data of three pigs. The inverse finite element solution that is used to determine both hyperelastic and viscoelastic material properties of pig liver is discussed in this chapter. In chapter 7, a linear viscoelastic FEM formulation is presented and a new superposition approach for the real-time execution of the linear viscoelastic model is proposed. In Chapter 8, the thesis is concluded with a summary of the performed work and future research studies.

Chapter 2

LITERATURE REVIEW

2.1 Minimally Invasive Surgery and Virtual Reality

Minimally Invasive Surgery (MIS) has been used increasingly for many surgical procedures over the last few years. In this new technology, surgeons use a small video camera connected to a video screen, and a few customized surgical tools to perform surgery with minimal tissue injury. The camera and instruments are inserted into the abdomen (laparoscopy) through small holes allowing the surgeon to explore the whole cavity without the need of making large standard openings dividing skin and muscle. Major advantages of this type of surgery to the patient are short hospital stay, timely return to work, and less pain and scarring after the surgery.

Although these advantages make MIS widespread, there are some difficulties associated with the use of this technology. Since surgeon manipulates organs from outside the body via instruments as he/she views his/her actions on a video display, he/she loses direct sense of touch and visual inspection. Because hand and eye coordination is difficult, surgeons need more training to successfully operate on patients. Training for laparoscopy relies on models, animals, and guidance from experienced surgeons in the operating room (O.R.) However, animal use is being reduced for ethical and cost reasons and also guidance in the O.R. presents danger to the patient. Models used in training can be grouped as mechanical models and virtual reality (VR) based models. In mechanical models, a simple box equipped with laparoscopic tools is used to grasp or cut different soft materials such as rubber. Although this training method is easy to carry out, it has many drawbacks like unrealistic representation of organs and surgery environment. In VR based models on the other hand, surgical procedures are simulated in multimodal virtual environments and visual and haptic feedback are provided to trainees. Although there are technical challenges in developing realistic simulations,

virtual reality based surgical simulators is a promising technology for training medical personnel [1-7]. The most significant challenge is the development of realistic soft tissue models. To meet this challenge, material properties of soft tissues must be determined and integrated into the tissue models.

2.2 Measurement of Soft Tissue Material Properties

Soft organ tissues exhibit complex nonlinear, anisotropic, nonhomogeneous, time, and rate dependent behavior. Fung [8] has revealed that a nonlinear stress-strain relationship is common for soft tissues but the degrees are different for different tissues. Since soft organs are composed of different materials, like elastin and collagen, in different combinations, hence, soft tissue properties are both coordinate and direction dependent. Time and rate dependent behavior is also common for soft tissues and explained by viscoelasticity. Time plays an important role in the behavior of soft organs. Since soft tissue material properties are extremely challenging to measure and model, several different measurement methods have been proposed in the literature [8, 10-19].

Methods for measurement of soft tissue material properties can be grouped into three classes according to measurement site as *in-vivo*, *in-situ,* and *in-vitro* (or *ex-vivo*). *In-vitro* or *ex-vivo* measurements are performed outside of body under well-defined boundary conditions using classical testing methods (i.e. tension or compression tests). Most tissue experiments conducted in the past have been *in-vitro* studies and the experimental data has been collected from the excised and shaped tissue samples [8, 17]. However, soft tissue material properties change in time and results obtained from *in-vitro* measurements can be misleading. Dead organ and muscle tissues typically stiffen with time. Furthermore, Ottensmeyer et al. [9] indicate that measurement environment of *in-vitro* studies does not represent the actual tissue conditions. For this reason, research has been recently focused on recording mechanical properties of soft tissues in a living state (*in-vivo*) and within a body (*in-situ*) [10-16, 18].

Soft tissue measurement techniques can also be grouped into two classes according to the amount of damage made on tissue during the measurements. In i*nvasive* methods, measurement is performed by entering into the body through puncture or incision. Because large openings allow insertion of test apparatus into the body easily, many different measurements were performed in literature invasively

[12, 14, 18]. However, this approach is not ideal for human experiments. On the contrary, *non-invasive* measurements are performed without making large incisions on the body. Most commonly, ultrasound waves are used to characterize tissue properties [19]. Although measurements made with an ultrasound allow *non-invasive* characterization, only the material properties in the linear range can be determined [11]. However, it is known that soft tissues show nonlinear force response to displacement stimulus. In *minimally invasive* approach, small incisions are made on the body and tissue damage is much less than the *invasive* method. Using this approach, a few groups have recently conducted animal and human experiments to characterize nonlinear and time-dependent material properties of soft tissues [10, 11, 13]. These measurements can be grouped into two: The first group of measurements what we call "free-form recording" requires a mechanical instrument equipped with position and force sensors, operator holding the probe manually indents tissue surface to measure force and displacement response [11, 12]. Carter et al. [12] conducted *ex-vivo* experiments with pig liver and *in-vivo* experiments with human liver using a hand-held probe. Kauer [11] performed tissue aspiration experiments using a hand-held instrument and collected data from pig kidney and human uteri. The second group of measurments involves a robotic arm and an end-effecter for making more controlled indentations [10, 13, 14, 18]. Brown et al. [10] used a laparoscopic grasper equipped with strain gages to measure grasping forces. They conducted *in-vivo* and *in-situ* experiments with porcine liver. Ottensmeyer [13] designed a robotic indenter to measure mechanical properties of pig liver during a minimally invasive surgery. His probe can make small indentations in the range of ±500µm. Tay et al. [14] programmed Phantom haptic device to achieve greater indentation depths up to 8 mm. The force response of pig liver to displacement stimulus is measured using a force sensor attached to the tip of the haptic interface. Later, Kim [20] analyzed the experimental data and estimated the Young Modulus of pig liver about 3 kPa based on the semi-infinite medium assumption. While the number of studies on *in-vivo* measurement of animal organ properties is increasing rapidly, there are only two studies available in the literature on humans [11, 12]. In both studies, force versus displacement data was collected using a hand-held probe.

In-vitro soft tissue measurements are performed in a laboratory environment using tissue samples of known geometries and standard mechanical tests. The characterization of material properties using the measurement data is relatively easy since cross-section of the sample, boundary conditions, and direction of loading are all set in advance. However, this is not the case with *in-vivo* or *in-situ* studies.

For this reason, an inverse solution is formulated to determine the unknown material properties from measured system response [29, 30, 31, 32, 33, 34]. An optimization routine is typically combined with a finite element method to match experimental data with the numerical solution through iterations.

2.3 Simulation of Soft Tissue Behavior

Virtual reality (VR) based surgical simulators that can provide the user with realistic visual and haptic feedback is a promising technology for training medical personnel. The core component of a computer-based surgical simulation and training system is the development of realistic organ-force models. A good organ-force model must reflect stable forces to a user, display smooth deformations, handle various boundary conditions and constraints, and show physics-based behavior in real-time. Although extensive research has been done on reality-based modeling of deformable tissues, integration of tissue properties into these models has been difficult due to the modeling challenges [1, 35]. Developing real-time and realistic organ-force models is challenging not only due to non-linearity, rate, and time dependence in material properties of organs but also due to layered and non-homogeneous structure of tissues. Furthermore, tool-tissue interactions generate dynamical effects and cause interactions of one organ with the others which are quite challenging to simulate in real-time [1]. Considering the fact that integration of incorrect tissue properties into deformable tissue models for simulation may cause adverse training effects, mechanical characterization of tissue properties is a requirement for a reality based surgical simulator to provide the user with the most accurate visual and haptic feedback.

In the past, significant efforts have been made to simulate soft tissue behavior in real-time [36, 37, 38, and 39]. There are currently two main approaches for developing force-reflecting organ models: particle-based methods [40, 5, 41, 42] and finite element methods [43, 44, 3, 38]. In particle-based models, nodes of an organ model are connected to each other with springs and dampers. Each node (i.e. particle) is represented by its own position, velocity, and acceleration and moves under the influence of forces applied by the surgical instrument [1]. Particle-based models can easily be constructed and simulated in real-time using today's typical desktop computers [45]. Cover et al. [41]

simulated deformation of a gallbladder using a simple surface-based mass-spring model. Bro-Nielsen et al. [5] implemented mass-spring models for the VR simulation of abdominal surgery. However, the application of particle-based models to simulation of soft tissue behavior is questionable because the integration of tissue properties into these models is not a trivial task. The spring and damping coefficients must be tuned to approximate the deformation physics of the organ and extracting these coefficients from material properties is not trivial. Construction of an optimal network of springs and dampers for a three-dimensional (3D) object is a complicated process. Finally, particle systems may become oscillatory or even go unstable under certain conditions [1, 45].

In finite element modeling (FEM), the geometric model of an organ is divided into surface or volumetric elements, properties of each element is formulated, and the elements are assembled together to study the deformation states of the organ for the forces applied by the surgical instruments. FEM-based models can display more realistic simulations then particle-based models and it is relatively easy to integrate measured tissue properties into FEM based models. However, their integration with medical simulators has been difficult due to real-time requirements. Simulating the real-time deformation dynamics of a FEM-based model is increasingly more difficult as the total number of nodes/degrees of freedom (dof) increase. With the addition of haptic displays, this has been even more challenging since a haptic loop typically requires a much higher update rate than a visual loop for stable force interactions [1, 46].

Both linear and non-linear FEM have been used in literature for modeling soft tissue mechanics. Linear elastic theory assumes linear material properties and models small deformations [45]. Achieving a computationally fast and stable simulation is possible with a linear FEM-based model since the stiffness matrix of the system is constant and the computations can be done in advance before running the simulation [52]. For this reason, most of the earlier FEM-based models have been linear [43, 44, 3, 48 and 38]. However, the assumptions of linearity and small deformations are not valid for human tissue having a complex non-linear behavior. Linear FEM cannot simulate non-linear tissue behavior and large deformations accurately for human tissues being exposed to large deformations up to 100% during an actual surgery [45, 47]. Non-linear FEM, on the other hand, models non-linearity of soft tissues and large deformations accurately [49, 6, 50 and 51]. While non-linear FEM-based models display more realistic deformation simulations than linear FEM-based

models, they have a much greater computational complexity due to non-constant stiffness matrix of the system [52].

FEM-based models can be grouped into static and dynamic models according to whether inertial and damping effects are taken into account or not in the model. Inertial and damping effects are neglected in static FEM while time dependence may (strictly-static) or may not be (quasi-static) considered [1]. In order to achieve real-time simulation rates with a continuum mechanics model, linear static finite element approaches have been used in most of the studies in the literature [53, 3]. Bro-Nielsen and Cotin [53] have shown that real-time simulation of a volumetric deformable model is possible using a quasi-static finite element method. Also, Cotin et al. [3] solved static equations of a nonlinear elastic tissue model using a modified finite element method. However, computationally efficient static FEM models can only simulate elastic behavior of soft tissues. On the other hand, dynamic FEM-based models can simulate influence of inertia and viscoelastic behavior of soft tissues [54].

Recently, a few studies have focused on real-time simulation of viscoelastic behavior [55, 35 and 56]. Debunne et al. [56] presented a robust, adaptive method for animating dynamic deformations of a visco-elastic object in real-time using an explicit finite element method. Hauth et al. [35] have proposed a new material description based on a mechanical quality factor for real-time simulation of viscoelastic tissue behavior. They employed a hierarchical basis using nested tetrahedral meshes to solve finite element formulations for viscoelasticity. Schoner et al. [55] introduced a method for simulating viscoelastic solids in real-time. Material properties were estimated from physical measurements of real objects. To model the viscoelastic effects, they replace the spring-like relations in the Discrete Green's Function Matrix (DGFM) with compositions of springs and dashpots. This provides the ability to simulate viscoelastic behavior while retaining the DGFM for primary deformation calculation. Although they achieved real-time rendering rates for visual display of deformations, a quasi-static elastic model has been utilized for calculating and displaying interaction forces reflected to a user via a haptic device.

Chapter 3

BASIC SOLID MECHANICS

3.1 Linear versus Nonlinear Mechanics

Fung [8] has shown that mechanical properties of soft tissues do not meet the definition of an elastic body. Similar to some materials such as elastomers, and polymers, soft tissues can undergo large deformations, and hence exhibit highly nonlinear behavior. The static behavior of many materials can be characterized by graphical representation of a load-deflection or force-displacement response as illustrated in Figure 3.1.

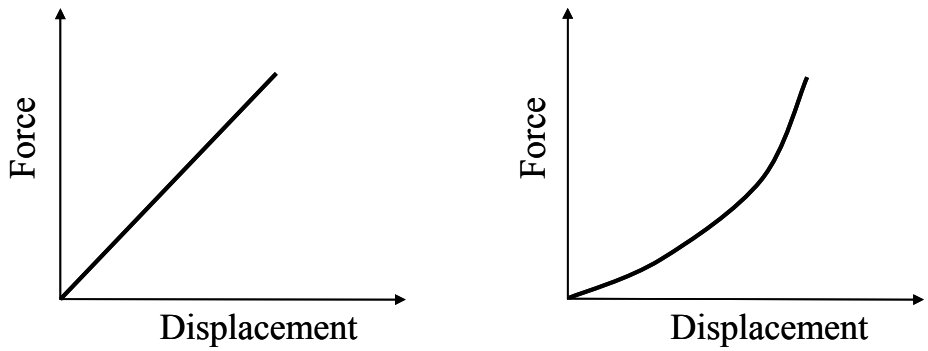

Figure 3.1: Force-displacement response: a) Linear behavior, and b) Nonlinear behavior

There are three major sources of nonlinear behavior: geometric nonlinearity, material nonlinearity, and boundary nonlinearity. The fact that the strain is a nonlinear function of the displacement is known as the geometric nonlinearity. The changes in the deformed shape are taken into account in the strain-displacement relation. In material nonlinearity, the constitutive equation (i.e.

stress-strain relation) is no longer linear. Material behavior depends on current deformation state and possibly past history of the deformation which may give rise to very complex phenomena such as *path dependence*, and *hysteresis* [65]. For some materials, the curve of stress versus strain in dynamic loading is not elliptical, but has pointed ends; this behavior is a manifestation of material nonlinearity [66]. The loop is called a *hysteresis* loop which represents a lag between cause and effect. Material nonlinearity can be grouped into two classes. The first one is time-independent behavior including hyperelasticity and plasticity, and the second is time-dependent behavior such as viscoelasticity and viscoplasticity. The details of viscoelasticity and hyperelasticity will be given in the following sections. Finally, boundary nonlinearity arises from dependency of applied forces and displacements on deformation of structure. Contact is a typical example of nonlinear boundary condition.

3.2 Introduction to Linear Viscoelasticity

A viscoelastic material is characterized by both elastic and viscous behavior. For a purely elastic material, all the energy stored in the sample during loading is returned when the load is removed. As a result, loading and response curves for elastic materials move completely in phase (Figure 3.2.a). A purely viscous material does not return the energy stored during loading (Figure 3.2.b). All the energy is lost as “pure damping” once the load is removed. These materials have only damping component and no stiffness component. Viscoelasticity is concerned with materials which exhibit both elastic and viscous behavior. Some of the energy stored in a viscoelastic system is recovered upon removal of the load, and the remainder is dissipated in the form of heat. Therefore, a phase difference occurs between loading and response curves (Figure 3.2.c) [23].

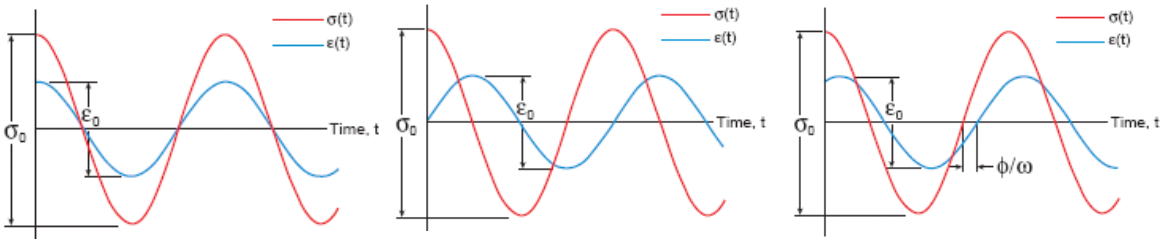

a) b) c)

Figure 3.2: Cyclic loading and response curves for various materials: a) Elastic material, b) Viscous material, and c) Viscoelastic material [23]

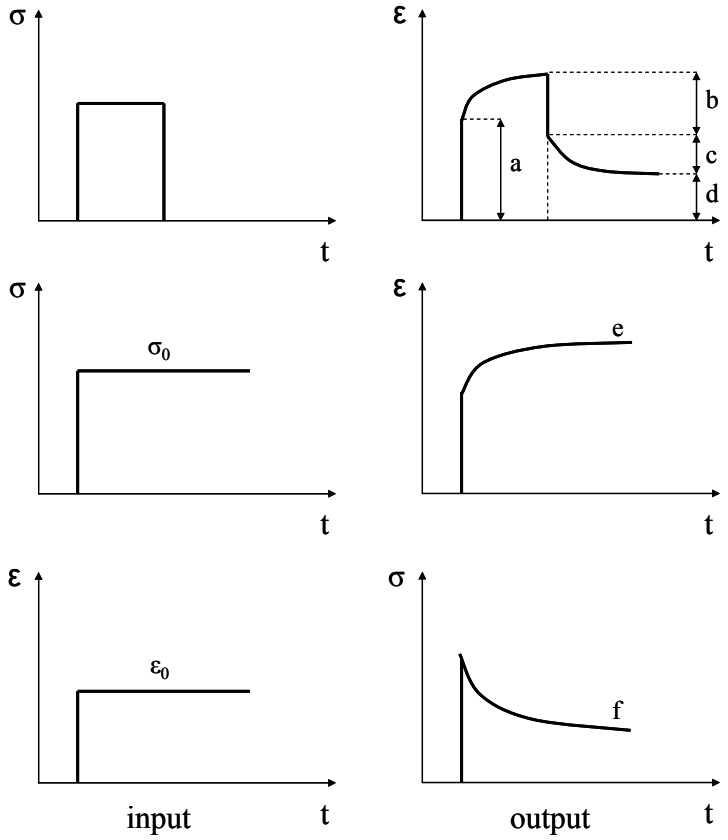

Figure 3.3: Viscoelastic phenomena: a. Instantaneous elastic response, b. Instantaneous elastic recovery, c. Delayed recovery, d. Permanent set, e. Creep under constant stress, f. Stress under constant strain [21].

In viscoelastic materials, an instantaneous elastic response is observed upon loading, and then a slow and continuous change in the response at a decreasing rate is obtained. When the load is removed a continuously changing response follows an initial elastic recovery as illustrated in Figure 3.3. Such viscoelastic materials are significantly influenced by the rate of straining or stressing; i.e., for example, the longer the time to reach the final value of stress at a constant rate of stressing, the larger is the corresponding strain [21]. Since time plays an important role in the behavior of viscoelastic materials, they are also called time-dependent materials. This time-dependency is explained by the phenomena of creep under constant stress and stress relaxation under constant strain as given in Figure 3.3.

Viscoelastic materials somehow keep a record of their response history and they are said to possess memory. This memory can clearly be seen in the constitutive relationship between the stress and strain tensors. As a result, mathematical models of viscoelastic behavior take the form of partial differential Volterra equation problems [22].

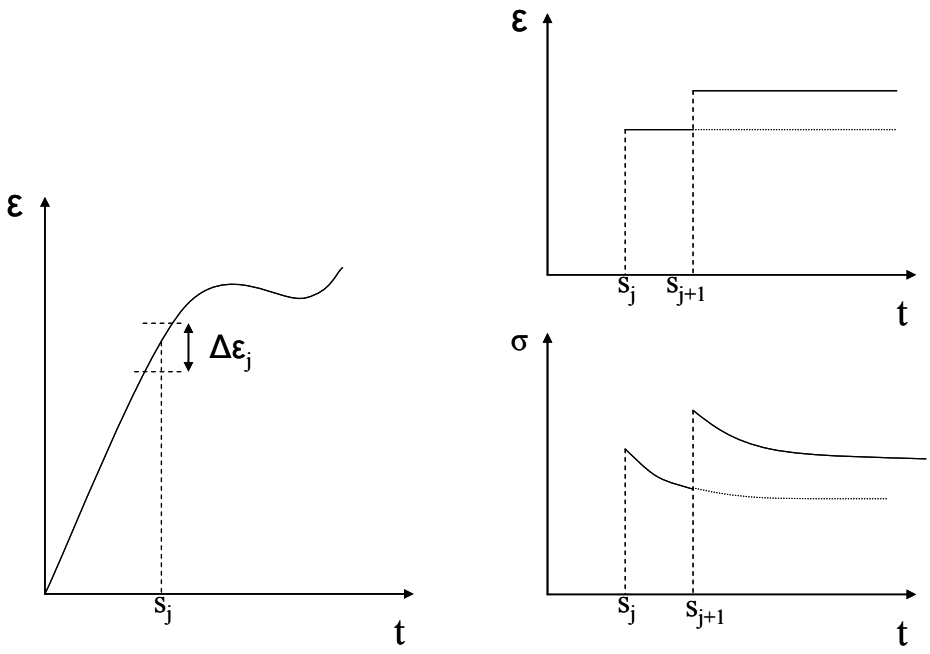

a) b)

Figure 3.4: a) Arbitrary strain input, and b) Boltzmann superposition principle

One way of deriving a constitutive relationship for linear viscoelastic materials is to assume that a Boltzmann superposition of strain increments can be applied to viscoelastic materials [22]. Consider an arbitrary strain input which is obtained through superposition of small strain increments (Figure 3.4) [21].

$$\varepsilon(t) = \sum_{j=1}^{n} \Delta\varepsilon_j = \int_0^t d[\varepsilon(s)] \tag{3.1}$$

These strain increments are related to corresponding stress increments by Hooke's law as follows

$$\sigma(t) = \sum_{j=1}^{n} \Delta\sigma_j (t - s_j) = \sum_{j=1}^{n} E(t - s_j)\Delta\varepsilon_j \tag{3.2}$$

Each of these stress increments also relax according to the time dependency of E (Figure 3.4.b). By taking appropriate limit, we get the following constitutive law

$$\sigma(t) = \int_0^t E(t - s)d[\varepsilon(s)] \tag{3.3}$$

If the strain history is differentiable, Equation 3.3 reduces to the following form

$$\sigma(t) = \int_0^t E(t - s)\frac{\partial\varepsilon(s)}{\partial s}ds \tag{3.4}$$

Time dependency of stress relaxation function E can be more conveniently given by spring and dashpot models. In these models, the stress carried by the spring is proportional to the strain in the spring and is given by Hooke's law (Equation 3.5). The stress carried in the dashpot is proportional to the strain rate and is given by Newton's law of viscosity (Equation 3.6). Viscoelastic materials then can be modeled as combination of springs and dashpots in series or parallel.

$$\sigma = E\varepsilon \tag{3.5}$$

$$\sigma = \eta \frac{d\varepsilon}{dt} \tag{3.6}$$

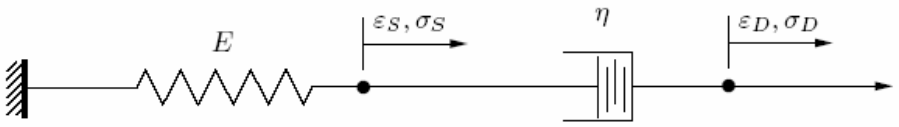

Figure 3.5: The Maxwell model [22]

The Maxwell model given in Figure 3.5 is a series connection of a spring and a dashpot. In this model ε_S and σ_S denote the strain and stress in the spring alone and ε_D and σ_D denote those in the dashpot alone [22]. Total strain in the Maxwell model is given by

$$\varepsilon = \varepsilon_S + \varepsilon_D \tag{3.7}$$

and if we differentiate both sides, we end up with

$$\frac{d\varepsilon}{dt} = \frac{1}{E}\frac{d\sigma_S}{dt} + \frac{\sigma_D}{\eta} \tag{3.8}$$

Since $\sigma = \sigma_S = \sigma_D$ then

$$\frac{d\sigma}{dt} + \frac{\sigma}{\tau} = E\frac{d\varepsilon}{dt} \tag{3.9}$$

where

$$\tau = \frac{\eta}{E} \tag{3.10}$$

is the so called relaxation time. Using $\sigma(0) = \varepsilon(0) = 0$, this ODE can be solved to give

$$\sigma(t) = \int_0^t E \exp(-\frac{t-s}{\tau}) \frac{\partial \varepsilon(s)}{\partial s} ds \tag{3.11}$$

and this is the scalar analogue of E in Equation 3.4 given by

$$E(t) = E \exp(-\frac{t}{\tau}) \tag{3.12}$$

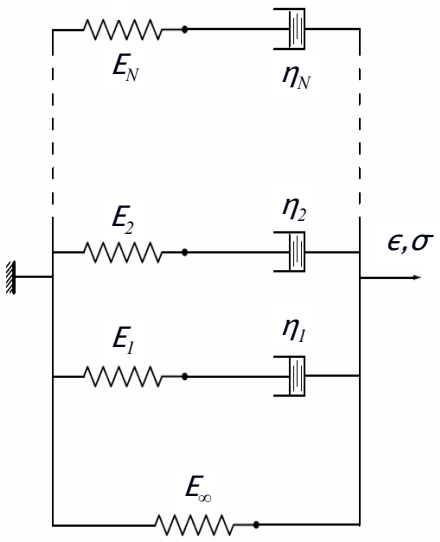

Figure 3.6: The generalized Maxwell solid, which is a combination of springs and dashpots with independent stiffness and viscosity parameters [22]

This derivation can be applied to Generalized Maxwell Solid element given in Figure 3.6 to end up with a Prony Series expression for relaxation function

$$E(t) = E_{\infty} + \sum_{j=1}^{N} E_j \exp\left(-\frac{t}{\tau_j}\right) \tag{3.12}$$

where, N is the number of the Maxwell elements (Figure 3.5) in generalized form, E_j is the independent stiffness parameter and τ_j is the relaxation time given in Equation 3.10.

3.3 Nonlinear Continuum Mechanics

In continuum mechanics, the initial or reference configuration of a body is defined by material (Lagrangian) coordinates $\boldsymbol{X}$ such that as the body deforms the coordinate axes deform with it. Similarly, the deformed or present configuration of the body is defined by spatial (Eulerian) coordinates $\boldsymbol{x}$ which is relative to a fixed reference Cartesian coordinate [24]. A main quantity in nonlinear continuum mechanics for strain definition is the deformation gradient tensor defined as

$$F_{ij} = \frac{\partial x_i}{\partial X_j} \tag{3.13}$$

The determinant of $\boldsymbol{F}$ is called the Jacobian of transformation relating undeformed volume V to deformed volume v as

$$dv = JdV \tag{3.14}$$

The deformation can be written as

$$x = X + u \tag{3.15}$$

where *u* represents the displacement field. The Right Cauchy-Green deformation tensor is defined as

$$C = F^T F \tag{3.16}$$

and the principle invariants are given as

$$\begin{aligned} I_1 &= trC \\ I_2 &= \frac{1}{2}\left[(trC)^2 - trC^2\right] \\ I_3 &= \det(C) \end{aligned} \tag{3.17}$$

Determinant of $\boldsymbol{C}$ is the measure of volume change, and for incompressible materials the third principle invariant, $\boldsymbol{I_3}$, is equal to 1. A measure of strain can be defined in terms of deformation tensor as

$$E = \frac{1}{2}(C - I) \tag{3.18}$$

where, E denotes the Lagrangian Green's strain tensor.

A body is called hyperelastic if it has a scalar function which stresses can be derived from. The function is called strain-energy function depending only on deformation gradient tensor, $\boldsymbol{F}$ [8, 67]. In linear continuum mechanics, the Cauchy stress tensor $\boldsymbol{\sigma}$ which is the true stress in the body and the strain tensor $\boldsymbol{\varepsilon}$ are used to describe constitutive equation. In nonlinear continuum mechanics, quantities are required that are invariant to rigid-body movements [25]. Two different stress tensors can be defined in addition to Cauchy stress tensor as

$$\begin{aligned} T &= JF^{-1}\sigma \\ S &= T\left(F^T\right)^{-1} \end{aligned} \tag{3.19}$$

where T is the first Piola-Kirchhoff Stress Tensor and S is the second Piola-Kirchhoff Stress Tensor. The second Piola-Kirchhoff stresses are directly related to strain-energy function as follows

$$S = \frac{\partial W}{\partial E} \tag{3.20}$$

where $\boldsymbol{E}$ is the Lagrangian Green's strain tensor given in Equation 3.18.

To describe a constitutive equation for hyperelastic materials, Equation 3.20 is used based on several strain-energy functions. If isotropy and incompressibility are assumed for soft tissues, hyperelasticity can be modeled using different strain-energy functions such as, neo-Hookean, Mooney-Rivlin, polynomial, Yeoh, Ogden and Arruda-Boyce. Some of the most common strain-energy functions are as follows

Neo-Hookean model: $$W = C_{10}(I_1 - 3) \tag{3.21}$$

Mooney-Rivlin model: $$W = C_{10}(I_1 - 3) + C_{01}(I_2 - 3) \tag{3.22}$$

Polynomial form: $$W = \sum_{i=0,j=0}^{N} C_{ij}(I_1 - 3)^i (I_2 - 3)^j \tag{3.22}$$

Yeoh model: $$W = \sum_{i=0}^{N} C_{i0}(I_1 - 3)^i \tag{3.22}$$

Ogden model: $$W = \sum_{i=1}^{n} \frac{\mu_i}{\alpha_i}(\lambda_1^{\alpha_i} + \lambda_2^{\alpha_i} + \lambda_3^{\alpha_i} - 3) \tag{3.22}$$

where C_{ij} and μ_i are material stiffness constants corresponding to Young's modulus in linear material. Except the Ogden model, above models are based on the principle invariants and the strain energy

function depends on the first and the second principle invariants (i.e. $W = f(I_1, I_2)$) due to incompressibility conditions. The Ogden model is directly based on principle stretch ratios, λ [60].

Chapter 4

ROBOTIC INDENTER

4.1 Design Considerations

One method to measure complex material behavior of soft tissues is to make mechanical indentations on tissue and record force response for further analysis. As it is mentioned in Chapter 2, there are two methods of measurement: a) free-form measurements and b) robotic measurements, which are both considered during the design stage of our measurement system.

A “free-form” measurement typically involves a hand-held probe equipped with position and force sensors. Major benefit of using a hand-held probe over a robotic arm is safety. Since the operator manually derives and positions the probe, unexpected and risky movements are unlikely to happen. However, there are two major problems with this design. First, the measurements are made manually and not repeatable. A load-cell which is triggered by the user can be used for actuation to achieve more controlled indentations [12]. The second difficulty is the identification of a reference point for displacement measurement. LVDTs (Linear Variable Differential Transformer) are typically used for position measurement. However, it is not easy to keep the probe stationary during measurements. For this reason, a reference point cannot be determined exactly for relative measurement of tissue displacements.

On the other hand, if a robotic arm is used for measurements, the problems related to actuation and displacement measurement can be solved. More controlled indentations can be made to tissue by a pre-programmed robotic arm. A robotic arm can be programmed to generate different types of stimuli. Thus, dependency to a user is eliminated and repeatability is achieved. Besides, end-effector position can be easily measured relative the coordinate frame attached to the base using encoders.

Other issues that must be considered in measurement of live tissue properties are sterilization, safety, and minimally invasive surgery (MIS) compatibility. Sterilization is carried out in the hospital with steam under pressure, liquid or gaseous chemicals, or dry heat [26]. Steam and ethylene oxide (gaseous) sterilization is performed at temperatures around 130^{o}C and 50^{o}C, respectively. On the other hand, liquid sterilization is performed at room temperature but takes longer time. Most sterilization techniques may easily damage the components of a robotic measurement system since sensors and actuators are sensitive to heat and humidity. Therefore, the design must enable the parts to be easily assembled and disassembled for sterilization.

Safety is the most important part of the design. A motion control algorithm must be implemented to make controlled indentations on tissue and to eliminate unexpected and risky movements. In addition, the indenter tip must not have any sharp edges to reduce damage to tissue during measurements.

Finally, the measurement system must be designed such that the measurements can be performed during a *minimally invasive surgery*. For that reason, parts of the indenter inserted into abdominal cavity must be compatible with laparoscopic tools and pass through standard surgical trocars (instruments that allow passage of laparoscopic tools). Also, contact between the indenter and the trocar during measurements must be reduced to eliminate measurement errors.

4.2 Design Details

Based on the requirements discussed above, we developed a robotic indenter to measure *in-vivo* material properties of soft tissues during a laparoscopic surgery. Our measurement system involves a haptic device programmed to make controlled indentations on tissue, a long laparoscopic indenter which can be inserted through a surgical trocar, and a force sensor attached to the indenter for the measurement of force response as shown in Figure 4.1. Using this system, we can make large indentations on internal organs in the abdominal region up to 10 mm. During the measurements, the haptic device functioned as a typical robotic manipulator and programmed to follow a predefined indentation trajectory in 3D space. Typically, haptic devices are used as human-computer interfaces and shipped with a software library that includes function calls for acquiring 3D position and

orientation of the end-effecter and for sending force and torque commands to the device. Making use of these function calls and an appropriate position control algorithm, one can program a haptic device to make static and dynamic indentations on soft tissue [27]. We used the Phantom haptic device (Model 1.0) from SensAble Technologies [68] as our robotic manipulator due to its versatility in position and velocity control in 3D space. The Phantom has a 13 x 18 x 25 mm workspace and its nominal position resolution is 0.03 mm. The Phantom was controlled by a personal computer via a software code written in C++ using the GHOST library.

To access the internal organs in the abdominal region during a laparoscopic surgery, a special purpose indenter was designed by paying attention to the assembly order (so that the indenter can be easily assembled and disassembled for sterilization) and to eliminate the friction between the trocar and the indenter. The indenter can be rigidly attached to the haptic device and it consists of two major parts: a laparoscopic probe fitted with a force/torque sensor and a cylindrical cover as shown in Figure 4.1. Both parts are separable into their sub-components for easy assembly after the sterilization. The assembly order of the indenter is given in Figure 4.1 and Figure 4.2. The laparoscopic probe is a long solid shaft with a diameter of 4 mm. The tip of the indenter is round to reduce the damage to tissue during indentations. A force-torque transducer (Nano 17 from ATI Industrial Automation) [69] is used for the purpose of measuring force response. The Nano 17 has a force range of $\pm$ 50 N in the x and y directions and $\pm$ 70 N in the z direction and has a resolution of 1/1280 N along each of the three orthogonal axes when attached to a 16-bit A/D converter. Data acquisition unit includes a 16-bit analog input card NI PCI-6034E (National Instruments) [70] with a maximum sampling rate of 200 kS/s.

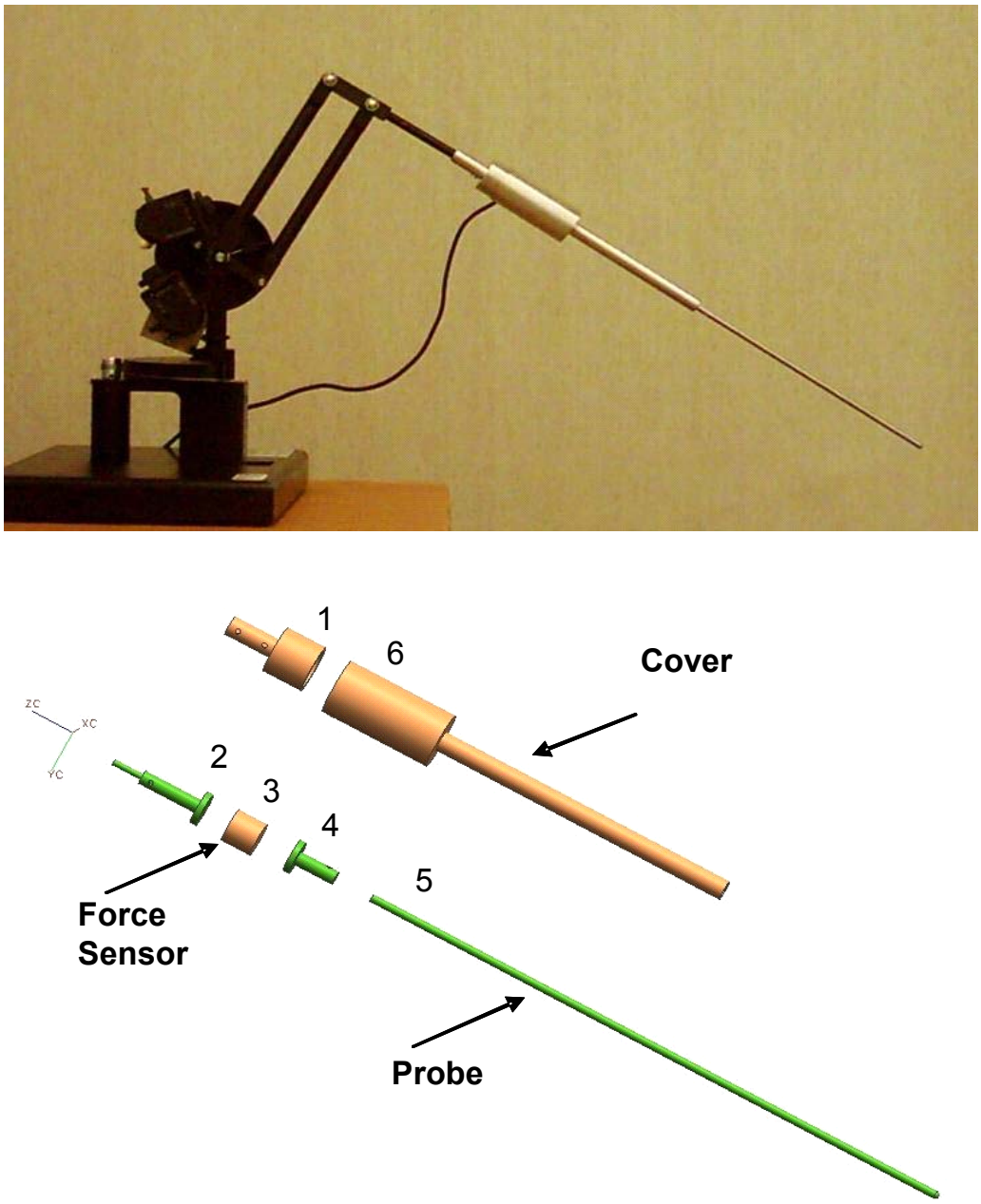

Figure 4.1: Our robotic indenter and its components. During the laparoscopic measurements, the indenter is inserted into the abdominal cavity through a surgical trocar. The cover prevents the probe and force transducer contacting the trocar during indentations. The numbers in the figure indicate the assembly order for sterilization purposes.

Figure 4.2: Attachment of the indenter to the robotic arm.

The cylindrical cover is a hollow shaft with two stages: the diameter of the first stage is sufficiently large enough so that the cover rests on the upper surface of a standard surgical trocar and the outer diameter of the second stage is small enough (10 mm) to insert it through the same trocar. The major role of the cover is to prevent the laparoscopic probe and the force sensor making contact with the trocar during measurements (see Figure 4.3). Otherwise, the friction between the trocar and the laparoscopic probe would cause measurement errors.

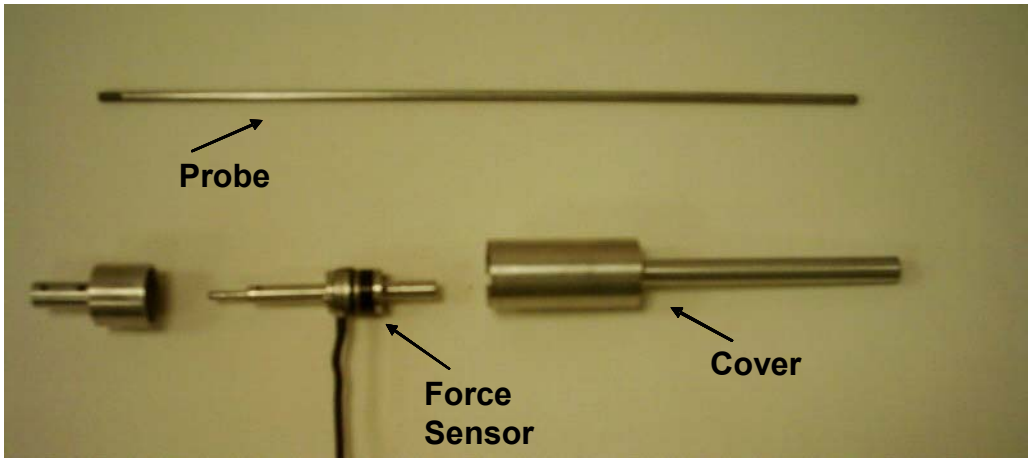

Figure 4.3: Components of the laparoscopic indenter.

4.3 Controller Design and GUI

A motion control algorithm must be implemented to make controlled indentations on tissue. Using software library of the Phantom haptic device, position and orientation of the end-effector can be obtained and force commands can be sent to control the device. Using this library and a PID controller, the indenter can be moved from an initial position to a desired position in 3D space in discrete time steps while compensating for positional errors. The block diagram of the controller is given in Figure 4.4.

A typical PID controller minimizes the error (E) between a desired variable and a system generated process variable creating an output based on the error. While the theory on PID controllers is well-established, there are different implementations in practice to reduce the error as discussed in [28]. We have experimented with many implementations and achieved the optimum results with the "trapezoidal integration". If we consider the desired position of the indenter as the set point (SP), the system generated position as the process variable (PV), and the output of the controller as the control variable (CV), the components of a PID controller with trapezoidal integration can be written as:

$$P(nT) = -K_P(PV(nT) - PV([n-2]T)) \tag{4.1}$$

$$I(nT) = K_I\left(\frac{T}{2}\right)(E(nT) + 2E([n-1]T) + E([n-2]T)) \tag{4.2}$$

$$D(nT) = -2K_D\left(\frac{1}{T}\right)(PV(nT) - 2PV([n-1]T) + PV([n-2]T)) \tag{4.3}$$

$$CV(nT) = CV([n-2]T) + P(nT) + I(nT) + D(nT) \tag{4.4}$$

where, K_P, K_D, and K_I are the proportional, derivative, and integral gains respectively.

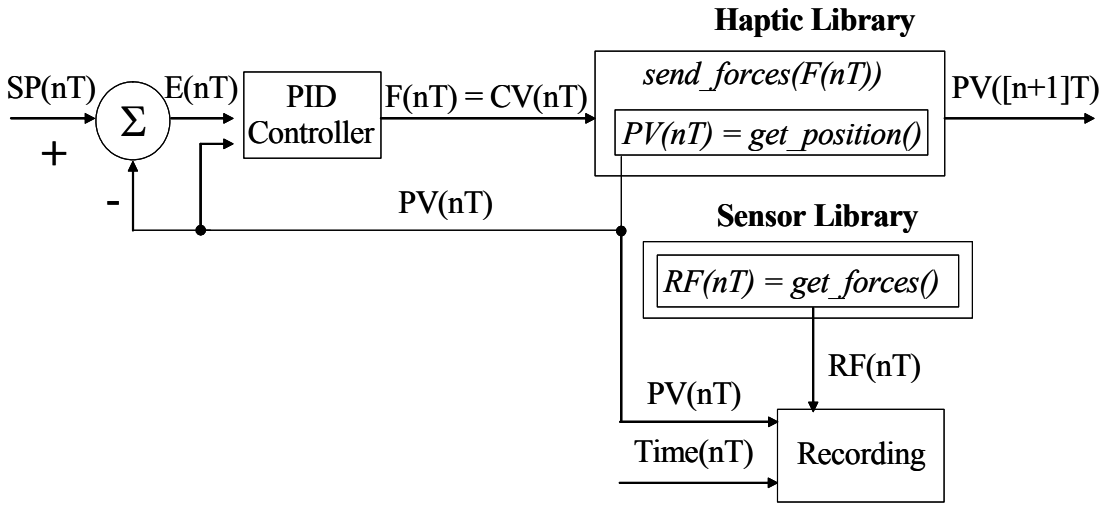

Figure 4.4: The block diagram of the controller.

The proper selection of controller gains is important for stable output and the minimization of the steady-state error. It is also important that the controller must be properly tuned for handling different loading conditions and material properties. We developed a methodological approach, similar to the well-known Ziegler Nichols approach, for tuning our control gains. First, the indenter is placed on the surface of the sample and K_P is set to a small value and the integral and derivative control actions are ignored by setting K_I and K_D to zero. Then K_P is increased with small increments until the system starts oscillating. At this stage, K_I is set to a small value and increased slowly until the system tracks the desired indentation trajectory successfully by reaching the goal point without any oscillation. Next, K_D is set to a small value and increased with small increments as long as the stability of the system keeps improving. As a last step, K_P and K_D are fine tuned until the force sensor produces an output with a least amount of noise. We tuned our controller gains on six different material samples having varying softness before the animal experiments. This process not only provided us with a general idea about the range of control gains, but also enabled us to construct a look-up table, which will be used to set the control gains for the future measurements.

We have developed a graphical user interface (GUI) to record current time, displacement and force data in a text file following each experiment. The GUI was written in MS Visual C++

environment using an ActiveX component to acquire force values from the sensor and the position values from the encoders at 1 kHz. Using the GUI, we can generate two different types of experimental stimuli: static and dynamic (sinusoidal). User can enter the values of stimulus parameters such as pre-indentation depth, rate of indentation, indentation depth, settling time, amplitude of indentation, stimulation time, and frequency of stimulation (see Figure 4.5).

The GUI also enables a user to load a predefined stimulus configuration from a file. Once the stimulus configuration is entered or loaded from a file and the indenter is placed on the surface of tissue, the GUI can send torque commands to the motors of the Phantom device to make controlled indentations (see Figure 4.6).

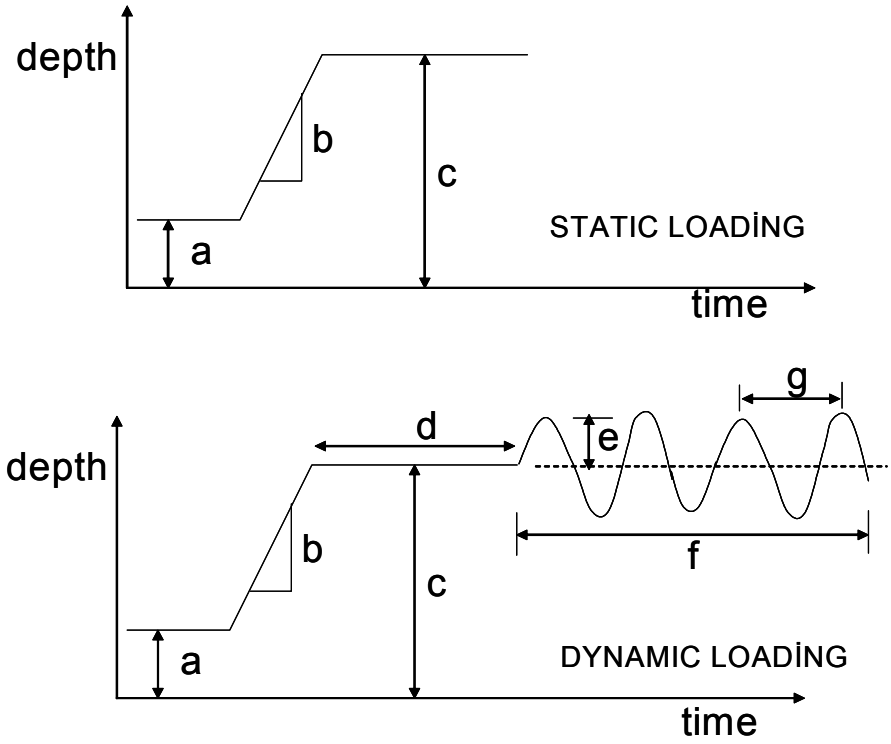

Figure 4.5: The profile of the static and dynamic stimuli (a: preindentation depth, b: rate of indentation, c: indentation depth, d: settling time, e: amplitude of stimulus, f: stimulation time, g: one period of stimulus).

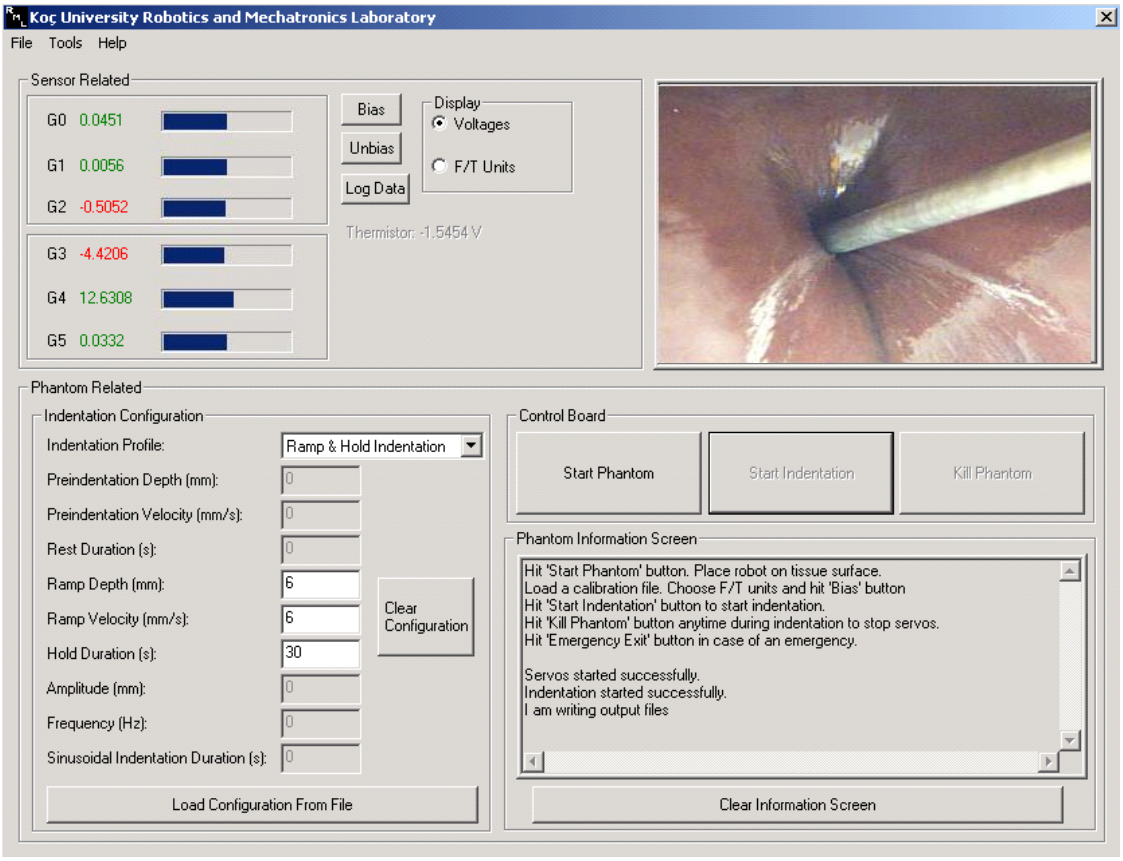

Figure 4.6: The graphical user interface (GUI) for generating a stimulus and recording experimental data.

4.4 Discussion

In comparison to the other measurement systems refered in the literature, our robotic measurement system is minimally invasive and designed to make controlled indentations on internal organs in the abdominal region during a laparoscopic surgery. Using this system, we can make large indentations, on internal organs in the abdominal region, up to 10 mm. And also, since our measurement setup is a controlled robotic system, both static and dynamic indentations can be performed. To test the functionality of the measurement system, preliminary experiments were

conducted using a mannequin and actual liver samples in our laboratory at Koc University (see Figure 4.7). Accuracy of the measurements was tested by a force measurement device.

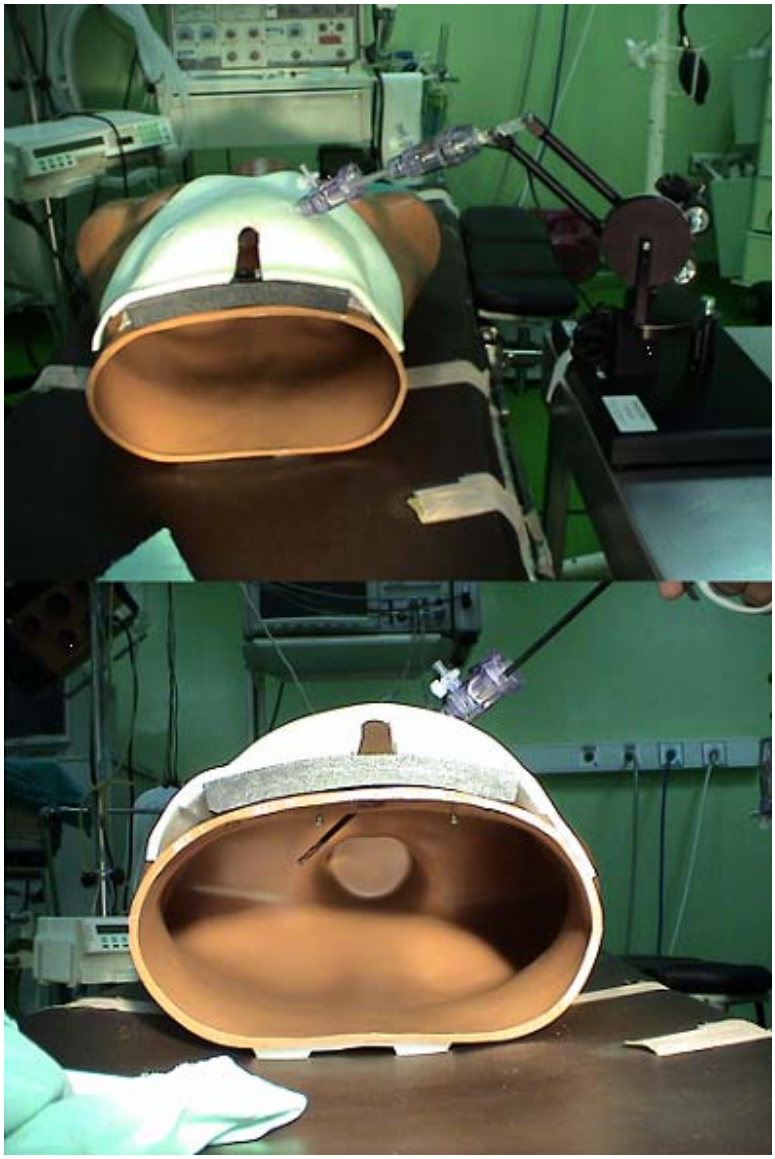

Figure 4.7: Preliminary experiments with the robotic indenter were conducted using a mannequin and liver samples in our laboratory at Koc University.

Chapter 5

ANIMAL EXPERIMENTS

5.1 Experimental Procedures

We conducted a series of *in-situ* animal experiments in collaboration with medical staff from Istanbul University, Department of Surgery (Faculty of Medicine) and Faculty of Veterinary Medicine in an operating room (see Figure 5.1). The experimental set-up and protocol were approved by the Faculty of Veterinary Medicine for use on pigs. Static and dynamic indentation experiments were conducted with three adult pigs to characterize the material properties of their liver.

Following the administration of anesthetic drugs, an incision was made in the abdominal area to insert a trocar. The abdominal cavity was inflated with carbon dioxide gas, in order to provide a working space and have a better vision of the cavity. Two additional trocars were placed on the abdominal wall to insert a small video camera and the indenter. Using an adjustable table and the camera, the orientation and the position of the indenter were adjusted so that the probe was always perpendicular to the surface of the liver (see Figure 5.2). Contact was made with thickest section of the liver.

Breathing causes movements of organs near the diaphragm and abdominal wall. Since these movements are not negligible considering the indentation displacements, assisted ventilation is usually applied for short period of times to perform *in-vivo* experiments [13, 14]. A chemical solution was administrated intravenously to put the animal to dead sleep after performing a few *in-vivo* measurements. The effect of breathing is shown in Figure 5.3 (see the difference between *in-vivo* and *in-situ* measurements).

As the indenter was inserted through one of the trocars, some leakage of carbon dioxide gas was observed through the holes of the indenter. The holes were covered by surgical tape and leakage was

stopped. Before the measurements start, preconditioning was applied to the liver to obtain repeatable results. The liver samples were preconditioned with 0.1 Hz dynamic loading for 60 seconds.

Figure 5.1: A view of the operating room during the animal experiments.

Figure 5.2: Video screen showing the pig liver and the indendation probe. The orientation and the position of the indenter were adjusted so that the probe was always perpendicular to the surface of the liver

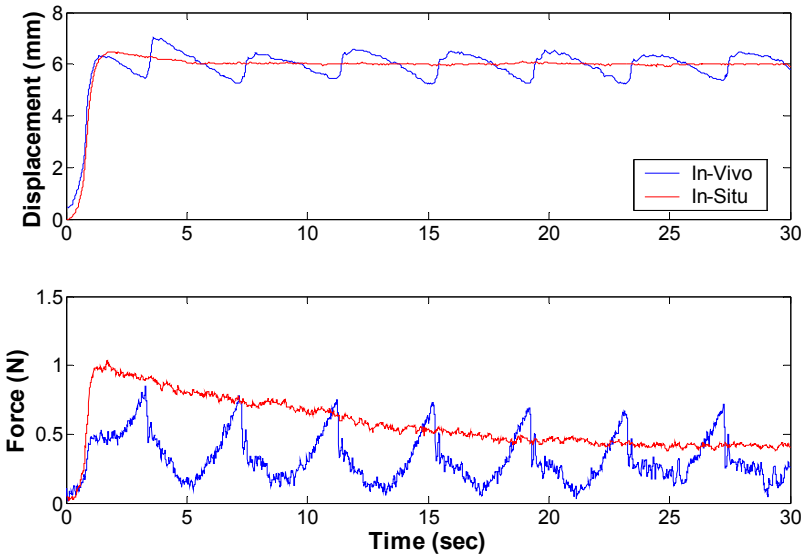

Figure 5.3: A comparison of *in-vivo* and *in-situ* measurements. Breathing causes excessive movement of the organ and disturbs the results.

5.2 Indentation Experiments and Experimental Results

After preconditioning the liver with 0.1 Hz dynamic loading for 60 seconds, three set of indentation experiments were performed in an hour: static indentation, stress relaxation, and dynamic indentation (sinusoidal stimulus).

5.2.1 Static Indentation

In static loading, the liver of each pig was indented slowly up to 10 mm of depth at a rate of 0.2 mm/s to characterize its force versus displacement response. In Figure 5.4, unfiltered results of 6, 8, and 10 mm static indentations pig # 2 are given. It can be seen that, data of the three different experiments match with each other quite well.

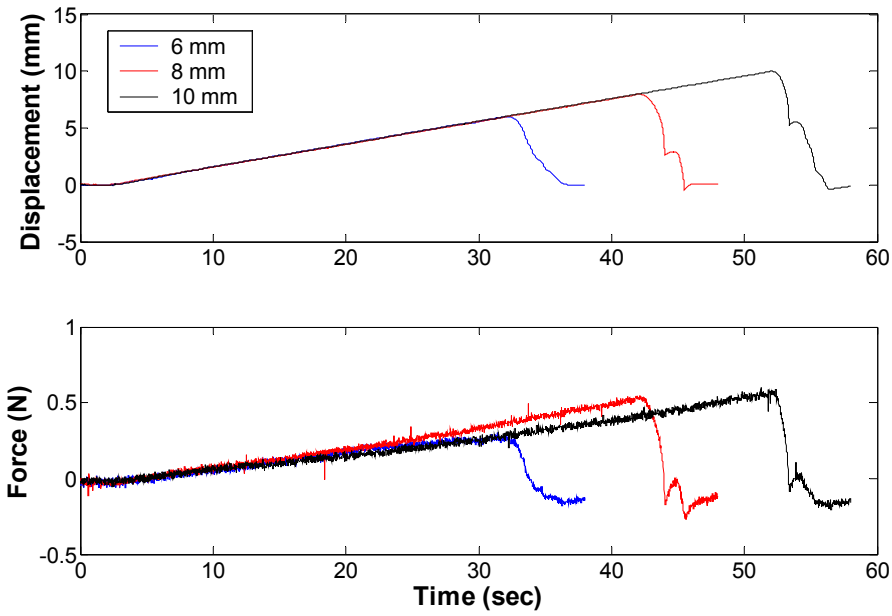

Figure 5.4: Displacement-time and force-time curves for static indentations of 6, 8, and 10 mm (strain rate is 0.2 mm/s) for pig #2.

The force-displacement response of pig liver for 8 mm static indentation is given in Figure 5.5. Data points are obtained using the mean values of three animals and variations are represented by vertical bars corresponding to the standard deviations. The force displacement relation is almost linear as shown in the figure.

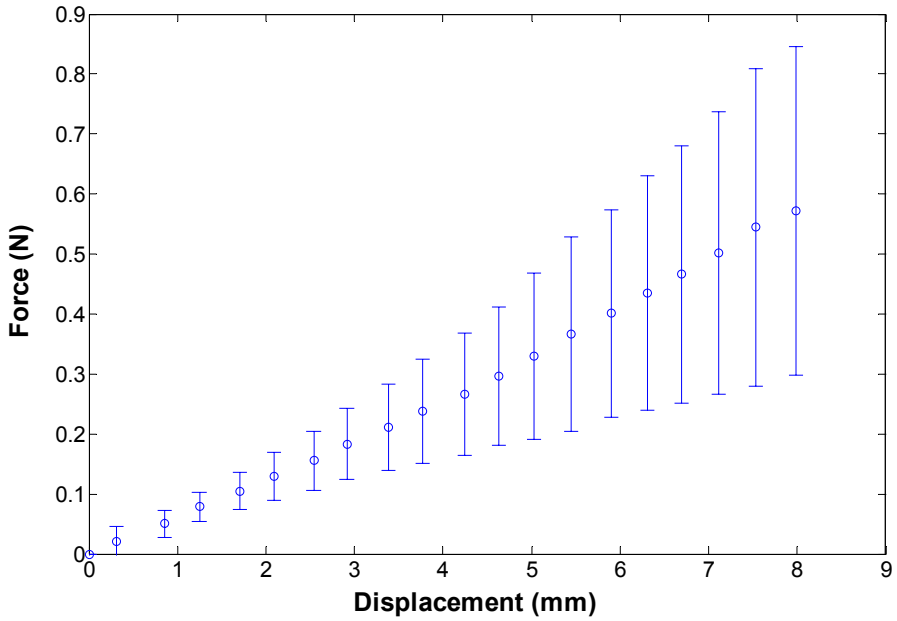

Figure 5.5: Force-displacement curve for static indentation of 8 mm (strain rate is 0.2 mm/s). Data points represent the mean values of three animals and vertical bars correspond to the standard deviations.

5.2.2 Stress Relaxation

In stress relaxation experiment, the liver of each pig was indented to the depths of 2, 4, 5, 6, and 8 mm in one second. After the fast indentation to predefined depth, the indenter was held there for 30 seconds to characterize the viscoelastic response of the liver. The step input assumption is used in the

analysis. The viscoelastic force relaxation response of the second pig liver for different indentations is given in Figure 5.6.

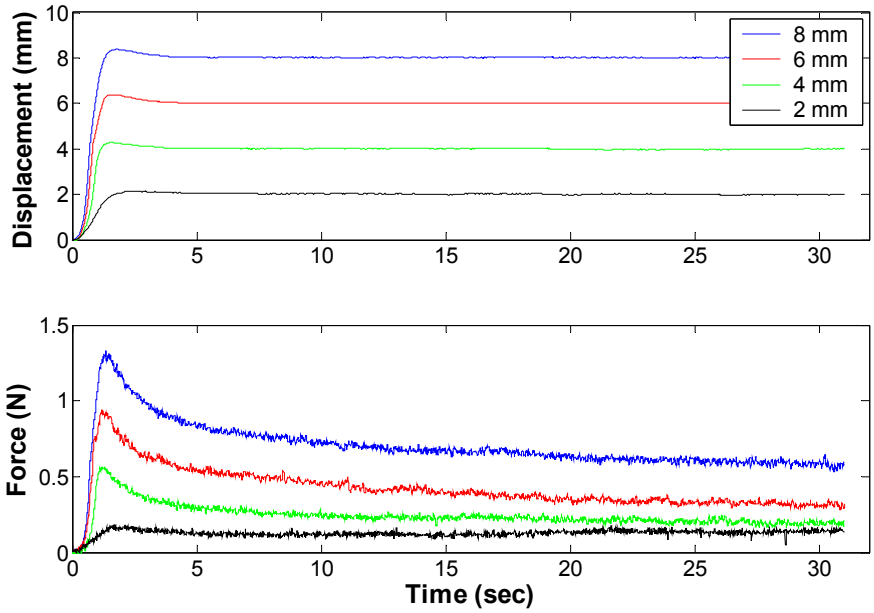

Figure 5.6: Displacement-time and force-time curves obtained from the stress relaxation data of pig #2 for 2, 4, 6, and 8 mm indentations at strain rates of 2, 4, 6, and 8 mm/s respectively.

Viscoelastic materials are significantly influenced by the rate of loading (i.e. strain rate). This phenomenon can be clearly seen in Figure 5.7. As the strain rate decreases, viscoelastic response disappears. To capture the whole stress relaxation behavior, high loading rates are required.

The force relaxation response of pig liver for 4 mm indentation is given in Figure 5.8. Data points are obtained using the mean values of three animals and the standard deviations are represented by vertical bars.

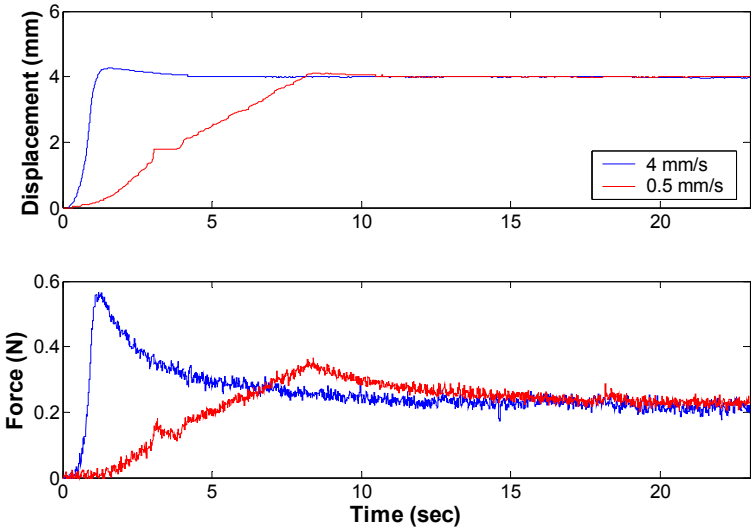

Figure 5.7: Displacement - time and force - time curves for two different loading rates. As the loading rate decreases, viscoelastic response disappears.

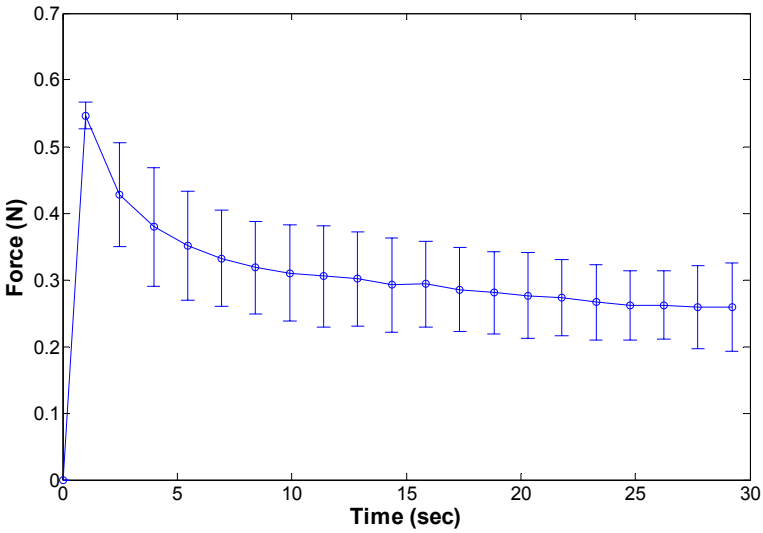

Figure 5.8: Force - time curve obtained from stress relaxation experiments for 4 mm indentation (strain rate is 4 mm/s). Data points represent the mean values of three animals and vertical bars correspond to the standard deviations.

5.2.3 Dynamic Indentation

In dynamic loading, sinusoidal indentations at frequencies of 0.05, 0.1, 0.2, 0.5, 1, 1.5, 2, and 3 Hz with an initial depth of 4 mm and amplitude of 1.5 mm were applied to the liver of each pig to characterize the changes in the relaxation modulus with respect to the frequency of stimulation. Durations of the sinusoidal indentations were determined according to have at least one complete cycle at each specific frequency. Figure 5.9 shows typical dynamic indentations and corresponding force response.

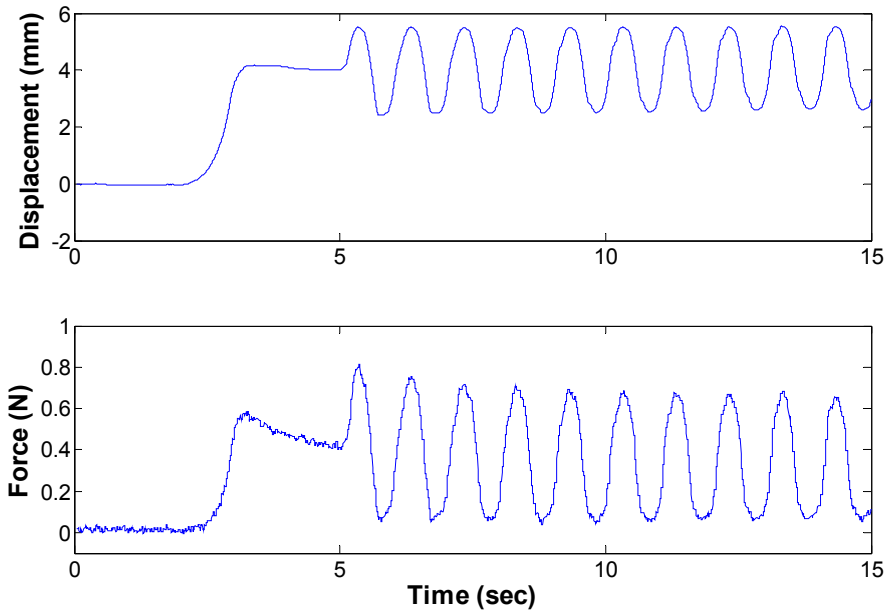

Figure 5.9: Sinusoidal indentation at frequency of 1 Hz and the corresponding force response of pig liver (pig #2) for an amplitude of 1.5 mm (initial indentation is 4 mm).

Chapter 6

CHARACTERIZATION OF SOFT TISSUE MATERIAL PROPERTIES

6.1 Elastic Contact Theory

The force-displacement response of pig liver for 8 mm static indentation is given in Figure 5.5. An effective shear and elastic modulus can be estimated from the data using the linear elastic contact theory and small deformation assumption. The effective shear modulus for small indentation of an elastic half-space by a rigid hemispherical indenter is given by Lee and Radok's solution [58]:

$$G = \frac{3P}{16\delta\sqrt{R\delta}} \tag{6.1}$$

where P is the force, δ is the indentation depth of a rigid sphere with a radius of R. From the relation between shear and elastic modulus for isotropic materials, effective elastic modulus can also be obtained:

$$E = 2G(1+\nu) \tag{6.2}$$

In the above relation, ν is Poisson ratio and it is equal to 0.5 for incompressible materials. Using Equations 6.1 and 6.2, the effective elastic modulus was estimated from experimental static indentation data for various indentation depths and is given in Table 6.1.

Table 6.1: Effective Young's modulus for different indentation depths

Indentation Depth δ [mm]	**Effective Young's Modulus E [kPa]**
2	16.9 ± 4.9
4	12.4 ± 4.1
6	10.8 ± 4.7
8	10.0 ± 4.7

6.2 Curve Fitting by MATLAB

The history of the stress response of viscoelastic materials is characterized by a function of time called "relaxation function", G(t). The relaxation function, typically, is represented by Prony series as follows [15]

$$G(t) = G_{\infty} + \sum_{k=1}^{N} G_k e^{-t/\tau_k} \tag{6.3}$$

where G_∞ is the long-term shear modulus and G_k and τ_k are the coefficients of the Prony series. Using the force relaxation data for 4 mm initial indentation, the coefficients of the Prony series were determined via curve fitting for N=2. We calculated the time varying shear modulus from the force response data using Equation 6.1. The coefficients of the relaxation function for three animals are given in Table 6.2. The force relaxation data of second test animal and the curve fitting results are given in Figure 6.1 for 4 mm indentation.

Table 6.2: The coefficients of the relaxation function

	Pig #1	**Pig #2**	**Pig #3**
G_1 [kPa]	2.402	3.688	0.827
G_2 [kPa]	1.733	2.495	3.333
τ_1 [s]	0.979	1.000	1.202
τ_2 [s]	5.650	9.000	10.641
G_∞ [kPa]	4.593	3.193	5.093

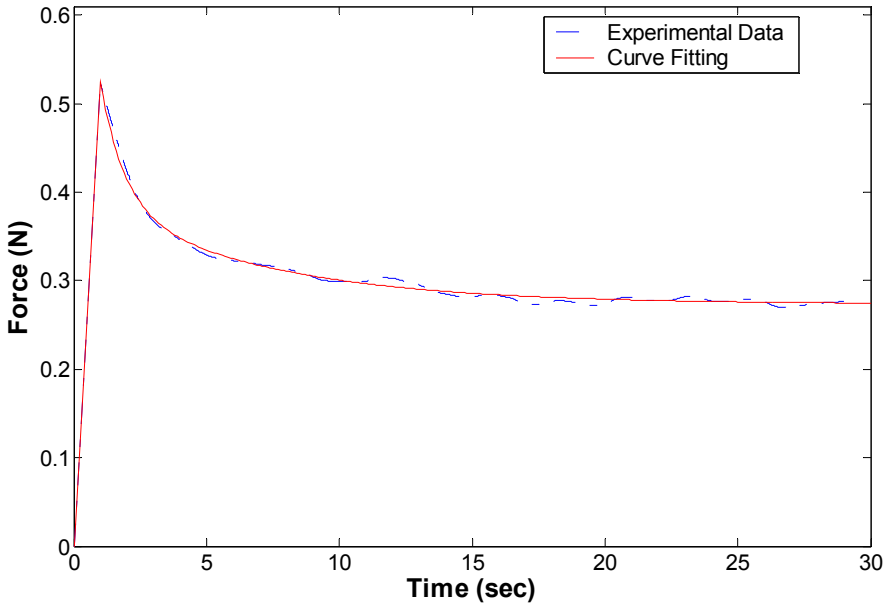

Figure 6.1: Experimental force relaxation curve for 4 mm indentation (strain rate is 4 mm/s) and curve fitting to the experimental data using Prony series.

Figure 6.2 shows the variation of the relaxation function with respect to time under three different initial conditions. As it is shown in Figure 6.2, the relaxation curves for different initial loadings almost overlap with each other, which is an indication of linear viscoelastic response [57].

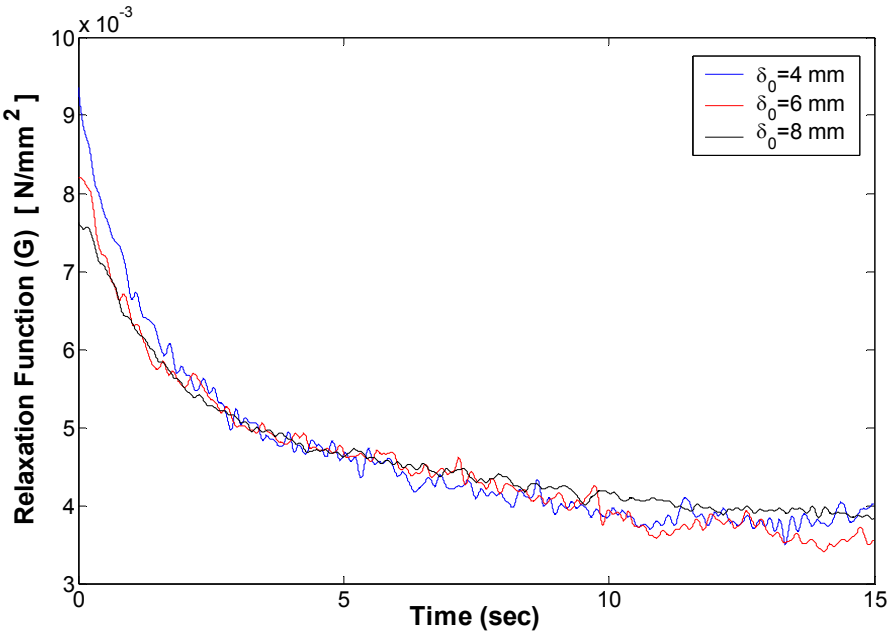

Figure 6.2: Relaxation modulus of a pig liver (pig #2) as a function of time for three different indentation depths.

6.3 Inverse Finite Element Solution

To extract the material properties of pig liver, we have developed an inverse finite element solution as outlined in Figure 6.3. The characterization of material properties based on experimental data is considered as the inverse problem. We used a finite element modeling package (ANSYS) and its optimization toolbox for solving the inverse problem. The assumptions made in the finite element model affect the quality of this solution [11].

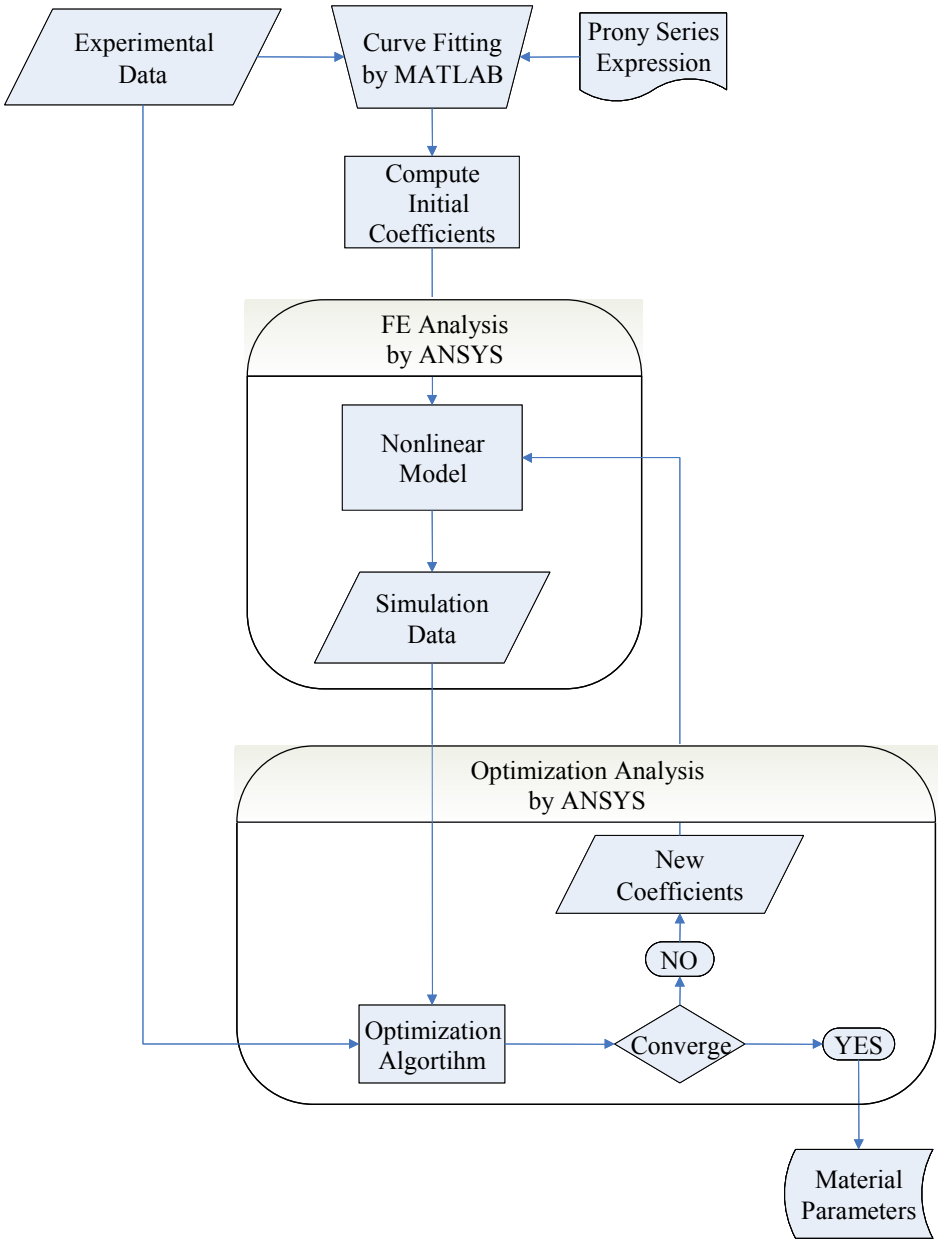

Figure 6.3: Flow chart of inverse finite element procedure.

6.3.1 Finite Element Modeling and Validation

Since the liver geometry is complicated and the boundary conditions are not well-known and also the performed indentations were small compared to the size of the liver, the liver tissue around the contact region was modeled using 2D axisymmetric finite elements in ANSYS. In order to validate this assumption, a series of calculations were carried out with the 2D FEM model using Lee and Radok's solution [58] for small indentation of an elastic half-space by a rigid hemispherical indenter. First, a 2D linear finite element model was constructed from eight-node quadratic axisymmetric elements (PLANE183) with linear material properties. The base and the lateral parts of the model was constrained. A frictionless contact between the rigid indenter and the FEM model was assumed. The indenter was also modeled using the same type of 2D linear finite elements. The elastic modulus of the indenter model was set to a high value of 2 GPa. Ratio of the indenter radius to the height of the FEM tissue model was set to a value of 0.1 to approximate the semi-infinite elastic half space. The value of Young's Modulus used in the tissue model was taken as 15 kPa from Table 6.1. To eliminate the effect of the geometry on small indentation calculations, the model was indented to a depth of 2 mm and the edges of the FEM model were widen up slowly until we reach a geometric size at which the change of error in force response was within an acceptable limit (i.e. less than five percent of the previous error). At the end of this process, the final dimensions of the 2D FEM model were 280 x 280 mm. In addition, mesh density was adjusted to reduce the number of finite element calculations. We started with a very fine mesh and then the elements that were far away from the contact region which had little effect on the calculations were slowly enlarged until the change of error in force response exceeded a threshold limit. As a result, an irregular grid density with an optimum number of interface (contact) elements was achieved. The final tissue model was made of 1363 finite elements in which 3 of them were contact elements (see Figure 6.4).

After obtaining an optimum geometry and mesh density for our model, a sensitivity analysis was performed to check the accuracy of the frictionless contact model. Contact is a highly nonlinear phenomenon and the contact stiffness (FKN) is the most important parameter affecting the accuracy and convergence of the finite element contact analysis [59]. The optimum value generating a converged solution with an acceptable level of accuracy is often problem dependent. FKN was chosen as 0.21 by trial and error such that the error in force response was minimum. As with the stiffness, the

penetration tolerance factor (FTOLN), which also affects the accuracy and convergence, was chosen as 0.1 by trial and error based on the same error criterion.

To simulate the nonlinear and viscoelastic effects, we again used the eight-node quadratic axisymmetric 2D elements but having hyperelasticity, viscoelasticity, large deflection, and large strain capabilities. The material properties of the tissue were assumed to homogeneous, isotropic, nonlinear (hyperelastic), time-dependent (viscoelastic), and nearly incompressible. In addition to the material nonlinearities, geometric nonlinearities were also taken into account by including large deformation and large strain effects. The Poisson's ratio was set to 0.49 to satisfy the incompressibility condition. Hyperelastic material behavior was modeled using Mooney-Rivlin strain-energy function given in Equation 3.22 The coefficients, C_{10} and C_{01}, were determined via the inverse solution. The stress relaxation function was modeled using 2-term Prony series. The equation for stress relaxation function given in ANSYS manual is slightly different than the equation presented in section 6.2. To begin with, the stress relaxation function for small strain viscoelasticity is given in ANSYS manual [60] as

$$G(t) = G_0\left(\alpha_\infty + \sum_{j=1}^{2} \alpha_j \exp\left(-\frac{t}{\tau_j}\right)\right) \tag{6.3}$$

where G_0 is the short-term shear modulus (i.e. initial modulus).

$$G_0 = G_\infty + \sum_{j=1}^{2} G_j \tag{6.4}$$

and α_j's are the relative moduli

$$\alpha_j = \frac{G_j}{G_0} \tag{6.5}$$

Using Equation 6.3, the deviatoric stress function can be shown as

$$s = \int_0^t 2G_0 \left[\alpha_\infty + \sum_{j=1}^{2} \alpha_j \exp\left(-\frac{t-\tau}{\tau_j} \right) \right] \frac{de}{d\tau} d\tau \tag{6.6}$$

The coefficients α_1, τ_1, α_2, τ_2, and the short-term shear modulus, G_0, are the input parameters entered in ANSYS. Therefore, the long-term shear modulus, G_∞, which is a dependent parameter, can be calculated as follows:

$$G_\infty = \left(1 - \sum_{j=1}^{2} \alpha_j \right) G_0 \tag{6.7}$$

Similar to Equation 6.6, the deviatoric stress expression is also formulated in ANSYS for large strain viscoelasticity

$$s = \int_0^t \left[\alpha_\infty + \sum_{j=1}^{2} \alpha_j \exp\left(-\frac{t-\tau}{\tau_j} \right) \right] \left(2 \frac{d}{d\tau} \frac{dW}{dC} \right) d\tau \tag{6.8}$$

where $\boldsymbol{W}$ is a strain energy function of a hyperelastic model, $\boldsymbol{C}$ is the right Cauchy-Green deformation tensor (see Equation 3.16). In ANSYS, the hyperelastic material coefficients of the strain energy function, C_{10} and C_{01}, correspond to the short-term response of the material. In order to calculate the long-term hyperelastic material coefficients, one should use the conversion factor of $\left(1 - \sum_{j=1}^{2} \alpha_j \right)$ as in Equation 6.7.

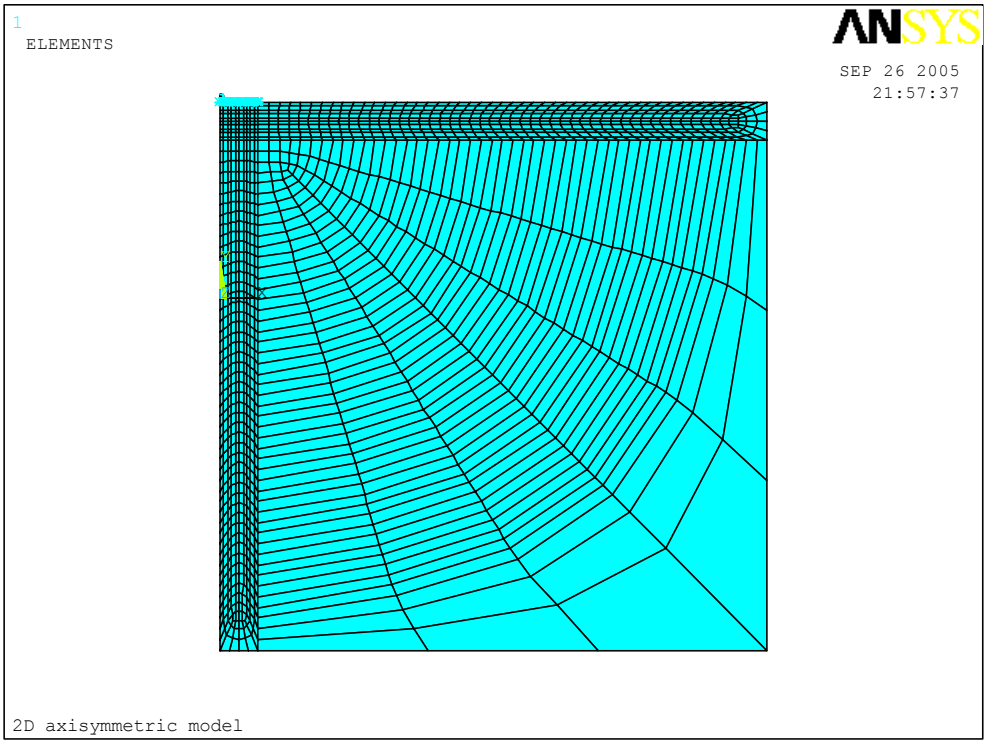

Figure 6.4: Mesh density of the 2D axisymmetric model. Mesh quality at the contact region is finer than the other parts.

6.3.2 Optimization Analysis by ANSYS

The ANSYS offers two optimization methods [60]: The *sub-problem approximation* method is an advanced zero-order method that can be efficiently applied to most problems. The *first-order* method is based on design sensitivities and is more suitable for problems that require high accuracy. Due to the high computational cost of the *first-order* method, the *sub-problem approximation* method is typically chosen for optimization. To perform an optimization in ANSYS, three set of variables must be defined. First set consists of independent quantities called *design variables* (*DVs*) to be determined by the optimization algorithm. Second set contains *state variables* (*SVs*) constraining the model. And

finally, a dependent variable (*objective function*) to be minimized must be determined. The *sub-problem* optimization algorithm uses approximations (curve fitting) to *SVs* and the *objective function* to determine the optimum values of *DVs*.

To calculate the hyperelastic and viscoelastic parameters of the liver tissue, C_{10}, C_{01}, α_1, τ_1, α_2 and τ_2 were assigned as *DVs*. 10 data points, (i.e. force samples representing the relaxation behavior), were chosen from the experimental force relaxation data and then compared with the force values (i.e. *SVs*) obtained from the finite element solution. The optimization algorithm minimizes the *objective function* defined as

$$Error = \sum_{j=1}^{10} \left(F_j^{EXP} - F_j^{FEM} \right)^2 \tag{6.9}$$

where F_j^{EXP} is the experimental force value of j^{th} data point and F_j^{FEM} is the force value obtained from the FEM simulation at the corresponding time.

Since convergence is highly depend on initial conditions and range of *design variables*, the initial values of α_1, τ_1, α_2 and τ_2 were taken from the experimantal data. Using the relation between Young's modulus and Mooney-Rivlin constants for incompressible materials under infinitesimal strain conditions [33],

$$E = 6(C_{10} + C_{01}) \tag{6.10}$$

the initial values of hyperelastic coefficients were determined by setting $C_{10} = C_{01}$.

6.3.3 Inverse FEM Results

Using the proposed inverse finite element solution, we estimated six material parameters: C_{10}, C_{01}, α_1, τ_1, α_2, and τ_1. The estimated material parameters of pig liver using the stress relaxation data of 4 mm indentation at a strain rate of 4 mm/s are given in Table 6.3 for three pigs.

Table 6.3: The estimated material properties of pig liver; α_j's and τ_j's are viscoelastic parameters and C_j's are hyperelastic parameters. Error was calculated using Equation 6.6.

	Pig #1		**Pig #2**		**Pig #3**	
	Initial Values	**Estimated Values**	**Initial Values**	**Estimated Values**	**Initial Values**	**Estimated Values**
α_1	0.275	0.271	0.393	0.466	0.089	0.369
α_2	0.199	0.267	0.266	0.241	0.360	0.114
τ_1 [s]	0.979	0.687	1.000	0.960	1.202	2.991
τ_2 [s]	5.650	4.299	9.000	8.440	10.641	11.791
C_{01} [kPa]	3.484	2.389	3.426	3.115	2.120	3.092
C_{10} [kPa]	3.484	3.490	3.426	3.443	2.120	2.300
Iterations	30		18		35	
Error	0.412E-03		0.282E-03		0.501E-03	

As discussed in section 6.3.1, the nonlinear elastic material coefficients, C_{10} and C_{01}, correspond to the short-term values and they are calculated based on the viscoelastic formulation given in ANSYS manual. These values must be multiplied by $\left(1-\sum_{j=1}^{2}\alpha_j\right)$ to convert them to long-term values.

Convergence behavior of each coefficient is given in Figures 6.5 and 6.6. A converged solution was obtained when all SVs were in the acceptable range of error (± 0.01 N). The finite element results and the experimental data are compared in Figures 6.7 and 6.8.

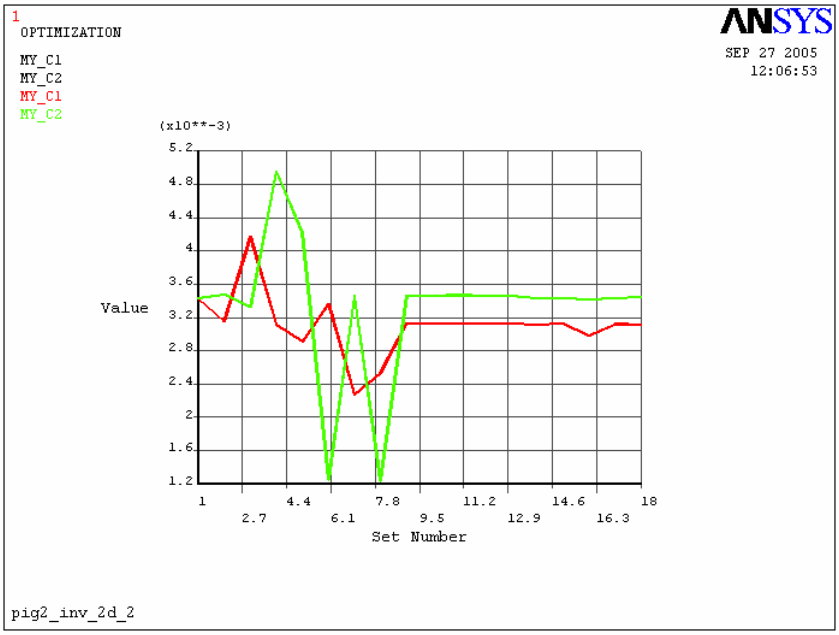

Figure 6.5: Convergence behavior of the Mooney-Rivlin parameters.

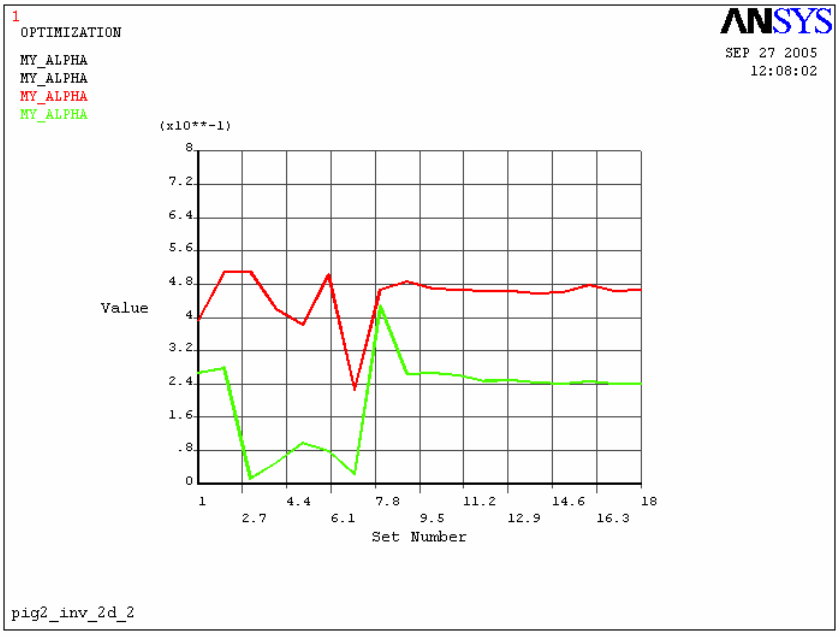

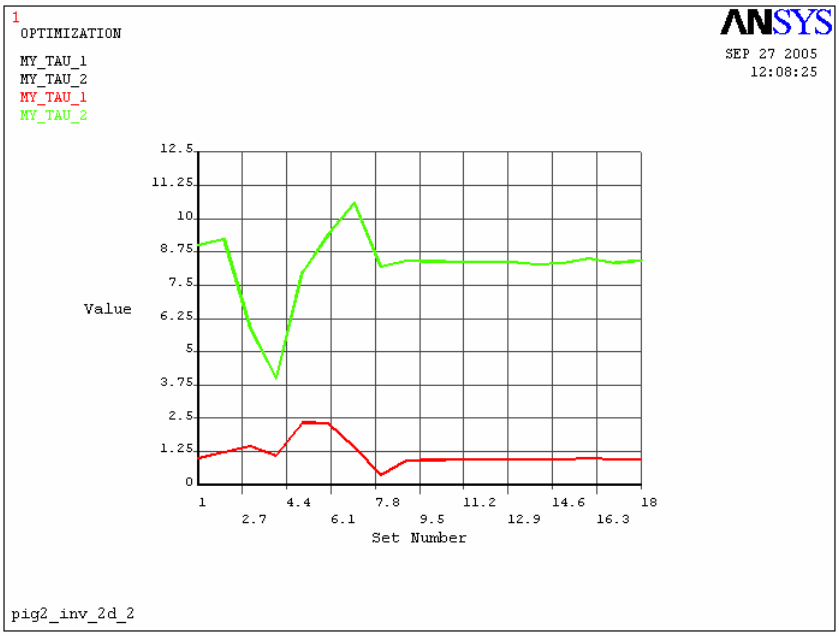

Figure 6.6: Convergence behavior of the viscoelastic parameters.

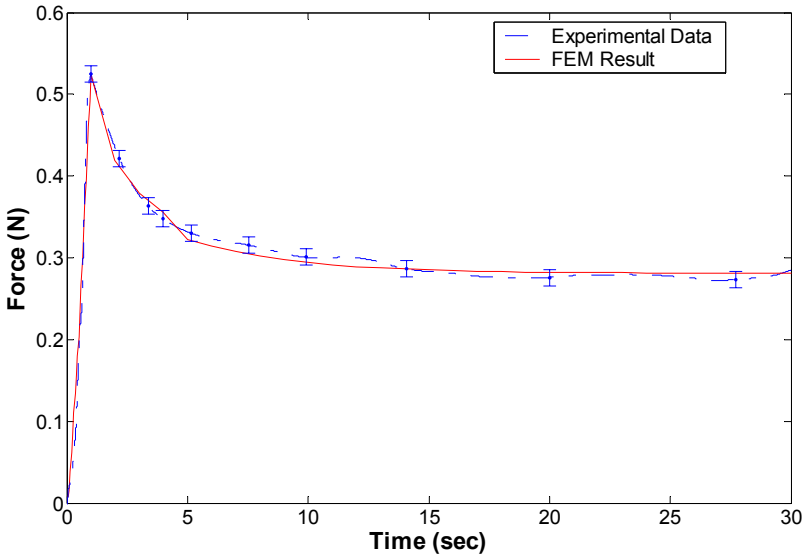

Figure 6.7: Experimental force relaxation curve for 4 mm indentation (strain rate is 4 mm/s) and the inverse FEM solution (pig #1). Vertical bars represent the allowable range of force error (± 0.01 N) for the inverse FEM solution

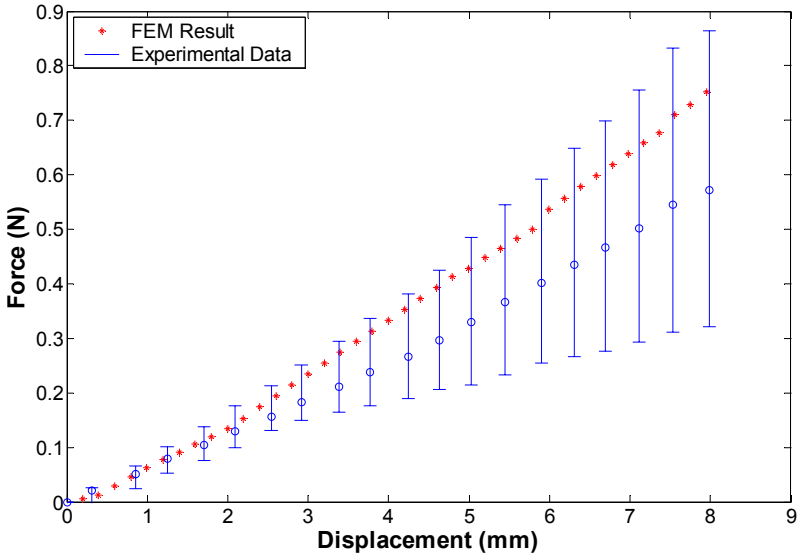

Figure 6.8: Force-displacement curve of three animals obtained by static indentation of 8 mm and the forward FEM solution for pig #1.

6.4 Discussion

In this chapter, we presented an inverse FEM solution for the characterization of material properties of soft tissues from experimental data. Using the experimental data of three pigs, we have estimated the viscoelastic and nonlinear hyperelastic material properties of pig liver. The estimated parameters can be used to develop realistic tissue models for surgical simulation. To simulate static tissue deformations using linear finite element models, we need to estimate Young's modulus (E) and Poisson's ratio (ν). In fact, soft tissues are almost incompressible ($\nu = 0.5$) and estimating the Young's modulus is sufficient. We estimated the Young's modulus using elastic contact models which are only valid for small deformations. Gefen and Margulies [15] have conducted experiments with soft gels and observed that the small deformation assumption is valid up to 4 mm indentations made with a semi-spherical probe of 2 mm radius. Our estimation of the Young' Modulus for porcine liver is around 15 kPa at this depth. A supporting value of 10-15 kPa was obtained by Ottensmeyer [13]. In addition, viscoelastic material coefficients were determined from the data of stress relaxation experiments via curve fitting to experimental data. Using Equation 6.3, the variation of the stress relaxation function was estimated as a function of time. There are three issues that should be considered in the analysis of data obtained through stress relaxation experiments. First, the stress relaxation function was obtained based on the small deformation assumption. Second, cut off time of the experiments affects the limiting value of the relaxation function. Third, representing an experimental data by sum of exponentials is not unique [8]. Finally, an inverse finite element solution was developed to determine the unknown material properties from the measured system response. Using an optimization method of the ANSYS, an inverse solution was developed for estimating the hyperelastic and viscoelastic material parameters of pig liver through iterations. Since the liver geometry and boundary conditions are not well known, the FEM model of the organ used in the inverse solution was validated using the Lee and Radok's solution [58] for small indentation of an elastic half-space by a rigid hemispherical indenter. Initial values and the constraints of the optimization were determined from the effective elastic modulus and the coefficients of stress relaxation function given in Section 6.1 and 6.2 respectively.

The simulation results of the inverse finite element procedure match with the experimental force relaxation data well. The coefficients of Prony series estimated through the inverse solution are

slightly different from the coefficients obtained through curve fitting to experimental data. This is due to the fact that only the relaxation component of the data was used in curve fitting (i.e. displacement input was assumed to be an ideal step function) and the elastic contact assumption was used in calculating the stress relaxation function. Using the estimated hyperelastic and viscoelastic parameters, the static indentation experiments were conducted in ANSYS to obtain a force versus displacement curve and compare it with the experimental force-displacement data. Although the force displacement response of pig liver matches with the response obtained from ANSYS for small indentations, it deviates slightly from the experimental data as the indentation depth increases. However, the simulated force response is still in the range of experimentally measured force response (Figure 6.8).

Chapter 7

REAL-TIME SIMULATION OF LINEAR VISCOELASTIC TISSUE BEHAVIOR

7.1 A numerical model for linear viscoelasticity

Kaliske and Rothert [61] propose a numerical scheme derived from the constitutive relation between stress and strain for linear viscoelastic materials as given in Equation 3.4. Splitting the integral in Equation 3.4 into elastic and viscoelastic contribution leads to

$$\begin{aligned}\sigma(t) &= \int_0^t E_\infty \frac{\partial \varepsilon(s)}{\partial s} ds + \int_0^t \sum_{j=1}^{N} E_j \exp\left(-\frac{t-s}{\tau_j}\right) \frac{\partial \varepsilon(s)}{\partial s} ds \\ &= E_\infty \varepsilon(t) + \sum_{j=1}^{N} \int_0^t E_j \exp\left(-\frac{t-s}{\tau_j}\right) \frac{\partial \varepsilon(s)}{\partial s} ds \\ &= \sigma_0(t) + \sum_{j=1}^{N} h_j(t)\end{aligned} \tag{7.1}$$

By defining time step as $\Delta t = t_{n+1} - t_n$, where t_{n+1} is the current time step, and substituting $\varepsilon(t) = \dfrac{\sigma_0(t)}{E_\infty}$ introduces a recursive formula for internal stress variables.

$$h_j(t_{n+1}) = \gamma_j \int_0^{t_{n+1}} \exp\left(-\frac{t_{n+1}-s}{\tau_j}\right)\frac{\partial\sigma_0(s)}{\partial s}ds$$

$$= \exp\left(-\frac{\Delta t}{\tau_j}\right)\gamma_j \int_0^{t_n} \exp\left(-\frac{t_n-s}{\tau_j}\right)\frac{\partial\sigma_0(s)}{\partial s}ds + \gamma_j \int_{t_n}^{t_{n+1}} \exp\left(-\frac{t_{n+1}-s}{\tau_j}\right)\frac{\partial\sigma_0(s)}{\partial s}ds \tag{7.2}$$

$$= \exp\left(-\frac{\Delta t}{\tau_j}\right)h_j(t_n) + \gamma_j \int_{t_n}^{t_{n+1}} \exp\left(-\frac{t_{n+1}-s}{\tau_j}\right)\frac{\partial\sigma_0(s)}{\partial s}ds$$

The transition from differential coefficient to discrete time steps yields

$$h_j^{n+1} = \exp\left(-\frac{\Delta t}{\tau_j}\right)h_j^n + \gamma_j \int_{t_n}^{t_{n+1}} \exp\left(-\frac{t_{n+1}-s}{\tau_j}\right)ds\,\frac{\sigma_0^{n+1}-\sigma_0^n}{\Delta t} \tag{7.3}$$

And the above expression is integrated analytically by Kaliske and Rothert [61] to end up with a recursive formula

$$h_j^{n+1} = \exp\left(-\frac{\Delta t}{\tau_j}\right)h_j^n + \gamma_j \frac{1-\exp\left(-\frac{\Delta t}{\tau_j}\right)}{\frac{\Delta t}{\tau_j}}\left[\sigma_0^{n+1}-\sigma_0^n\right] \tag{7.4}$$

By introducing tensor quantities, Equation 7.1 can be extended to a 3D approach. The total stresses of a linear elastic Maxwell-material

$$\boldsymbol{\sigma}^{n+1} = \boldsymbol{\sigma}_0^{n+1} + \sum_{j=1}^{N} \boldsymbol{h}_j^{n+1} \tag{7.5}$$

are determined from the elastic contribution and internal stress variables

$$\boldsymbol{h}_j^{n+1} = \exp\left(-\frac{\Delta t}{\tau_j}\right)\boldsymbol{h}_j^n + \gamma_j \frac{1-\exp\left(-\frac{\Delta t}{\tau_j}\right)}{\frac{\Delta t}{\tau_j}}\left[\boldsymbol{\sigma}_0^{n+1} - \boldsymbol{\sigma}_0^n\right] \tag{7.6}$$

7.2 Linear Static FEM formulation

We represent the object model, **Ω**, in terms of finite number of elements to be able to find the solution to the deformation problem using the potential energy equilibrium of each element. We have chosen to use four-node tetrahedrons with linear interpolation functions.

Bro-Nielsen and Cotin [53] discretized **Ω** in the form of tetrahedrons each having nodes P_q defined by $\boldsymbol{x_q} = [x_q\ y_q\ z_q]^T$. The deformation vector $\boldsymbol{u}_q = [u_q\ v_q\ w_q]^T$ specifies the displacement of each node. ${}_eP_i$ denotes the nodes of each tetrahedral finite element, ${}_e\Omega$, where i is the local number of the node varying between 1 and 4.

The linear interpolation of the displacement field between the nodes of each tetrahedron is

$$\boldsymbol{u(x)} = \sum_{i=1}^{4} {}_eN_i\ (\boldsymbol{x})\,{}_e\boldsymbol{u}_i \tag{7.7}$$

where ${}_eN_i\ (\boldsymbol{x})$ are the basis functions and defined as the natural coordinates of the tetrahedron.

The total potential energy of the system is given by

$$\Pi = \frac{1}{2}\int \boldsymbol{\sigma}^T \boldsymbol{\varepsilon} d\,{}_eV - \Pi_{ext} \tag{7.8}$$

where Π_{ext} is the work done by external forces and ${}_eV$ is the volume of each element. The solution to the deformation problem of a linear elastic material can be found when the potential energy of the

system reaches its minimum value. To find the minimum value, the derivative of the potential energy is taken with respect to displacement vector.

With known displacements within the element, the strains at any point can be determined by the following relation [62]

$$\boldsymbol{\varepsilon} = {}_e\boldsymbol{B}\,{}_e\boldsymbol{u} \tag{7.9}$$

where ${}_e\boldsymbol{B}$ is the constant matrix obtained by the basis functions ${}_eN_i$ ($\boldsymbol{x}$):

$${}_e\boldsymbol{B} = \begin{bmatrix} \frac{\delta}{\delta x} & 0 & 0 \\ 0 & \frac{\delta}{\delta y} & 0 \\ 0 & 0 & \frac{\delta}{\delta z} \\ \frac{\delta}{\delta y} & \frac{\delta}{\delta x} & 0 \\ \frac{\delta}{\delta z} & 0 & \frac{\delta}{\delta x} \\ 0 & \frac{\delta}{\delta z} & \frac{\delta}{\delta y} \end{bmatrix} \tag{7.10}$$

Assuming a linear behavior, the stress-strain relation is given by Hooke's law as

$$\boldsymbol{\sigma} = \boldsymbol{C}_{elastic}\,\boldsymbol{\varepsilon} \tag{7.11}$$

where $\boldsymbol{C}_{elastic}$ is a symmetric 6x6 material stiffness matrix. It is defined by the two Lamé constants μ and λ for a homogeneous and isotropic material as the following:

$$\boldsymbol{C}_{elastic} = \begin{bmatrix} \lambda+2\mu & \lambda & \lambda & 0 & 0 & 0 \\ \lambda & \lambda+2\mu & \lambda & 0 & 0 & 0 \\ \lambda & \lambda & \lambda+2\mu & 0 & 0 & 0 \\ 0 & 0 & 0 & \mu & 0 & 0 \\ 0 & 0 & 0 & 0 & \mu & 0 \\ 0 & 0 & 0 & 0 & 0 & \mu \end{bmatrix} \tag{7.12}$$

First Lamé constant (μ) is also known as shear modulus (G) and λ is the second Lamé constant given as

$$\mu = G = \frac{E}{2(1+v)} \tag{7.13}$$

$$\lambda = \frac{Ev}{(1+v)(1-2v)} \tag{7.14}$$

where E is Young's Modulus and v is Poisson's Ratio.

Using Equations 7.9 and 7.11 and taking the derivative of Equation 7.8 with respect to displacement vector, the equilibrium potential energy equation for each linear elastic element can be rewritten as

$$\int_e \boldsymbol{B}^T \boldsymbol{C}_{elastic}\, {}_e\boldsymbol{B}_e \boldsymbol{u} dV - {}_e\boldsymbol{f} = \boldsymbol{0} \tag{7.15}$$

where ${}_e\boldsymbol{f}$ is the discretized force vector for the element.

Using stress force term definition given in [62] as

$$\begin{aligned} \boldsymbol{F}_{int} &= \int \boldsymbol{B}^{T} \boldsymbol{\sigma} dV \\ &= \left(\int \boldsymbol{B}^{T} \boldsymbol{C}_{elastic} \boldsymbol{B} dV \right) \boldsymbol{U} \\ &= \boldsymbol{K}\boldsymbol{U} \end{aligned} \tag{7.16}$$

we end up with the famous linear finite element equation

$$_{e}\boldsymbol{K}_{e}\boldsymbol{u} = _{e}\boldsymbol{f} \tag{7.17}$$

7.3 Linear Viscoelastic FEM formulation

To derive a similar expression for linear viscoelastic finite element model, using relations in Equations 7.9 and 7.11 and the elastic contribution term

$$\boldsymbol{\sigma}_{0}^{n+1} = \boldsymbol{C}_{elastic}\, \boldsymbol{\varepsilon}^{n+1} \tag{7.18}$$

Equation 7.5 can be written as

$$\begin{aligned} \boldsymbol{\sigma}^{n+1} &= \boldsymbol{C}_{elastic}\boldsymbol{B}\boldsymbol{U}^{n+1} + \sum_{j=1}^{N}\left[\exp\left(-\frac{\Delta t}{\tau_j} \right) \boldsymbol{h}_j^{n} + \gamma_j A_j \left(\boldsymbol{C}_{elastic}\boldsymbol{B}\boldsymbol{U}^{n+1} - \boldsymbol{C}_{elastic}\boldsymbol{B}\boldsymbol{U}^{n} \right) \right] \\ &= \boldsymbol{C}_{elastic}\boldsymbol{B}\left(1 + \sum_{j=1}^{N} \gamma_j A_j \right) \boldsymbol{U}^{n+1} + \sum_{j=1}^{N} \exp\left(-\frac{\Delta t}{\tau_j} \right) \boldsymbol{h}_j^{n} - \boldsymbol{C}_{elastic}\boldsymbol{B}\left(\sum_{j=1}^{N} \gamma_j A_j \right) \boldsymbol{U}^{n} \end{aligned} \tag{7.19}$$

where

$$A_j = \frac{1 - \exp\left(-\frac{\Delta t}{\tau_j}\right)}{\frac{\Delta t}{\tau_j}} \tag{7.20}$$

τ is one of the coefficients of the relaxation function of Prony Series. Using the stress force term definition given in Equation 7.16, the internal force expression is derived from Equation 7.19

$$\boldsymbol{F}_{int}^{n+1} = \boldsymbol{K}_T \boldsymbol{U}^{n+1} + \boldsymbol{H}^{n+1} - \boldsymbol{K}_{hist} \boldsymbol{U}^n \tag{7.21}$$

where $\boldsymbol{K_T}$ is the constant tangent stiffness matrix, $\boldsymbol{U}^n$ is vector of nodal displacements at previous time step n, $\boldsymbol{K_{hist}}$ is the history stiffness matrix, and $\boldsymbol{H}^{n+1}$ is the history matrix at current time step $n+1$. By introducing following equality

$$\boldsymbol{F}_{int}^{n+1} = \boldsymbol{F}_{ext}^{n+1} \tag{7.22}$$

we end up with a most general numerical expression for linear viscoelasticity

$$\boldsymbol{K}_T \boldsymbol{U}^{n+1} = \boldsymbol{F}_{ext}^{n+1} - \boldsymbol{F}_{hist}^{n+1} \tag{7.23}$$

where internal load history vector of the object at time step n is

$$\boldsymbol{F}_{hist}^{n+1} = \boldsymbol{H}^{n+1} - \boldsymbol{K}_{hist} \boldsymbol{U}^n \tag{7.24}$$

Solving Equation 7.23 for $\boldsymbol{U}^{n+1}$, we get the expression for computing nodal displacements of a viscoelastic object under the influence of internal load history and the external load at a particular time, $n+1$, as

$$\boldsymbol{U}^{n+1} = \boldsymbol{K}_{\boldsymbol{T}}^{-1}\left[\boldsymbol{F}_{\boldsymbol{ext}}^{n+1} - \boldsymbol{F}_{\boldsymbol{hist}}^{n+1}\right] \tag{7.25}$$

Tangent stiffness matrix is obtained from the element tangent stiffness matrices via assembly

$$\boldsymbol{K}_{\boldsymbol{T}} = \mathrm{A}_{e=1}^{Ne}({}_{e}\boldsymbol{K}_{\boldsymbol{T}}) \tag{7.26}$$

where N_e is the number of elements. Using Equations 7.16 and 7.19, ${}_{e}\boldsymbol{K}_{\boldsymbol{T}}$, the tangent stiffness matrix of each element, is derived as follows

$${}_{e}\boldsymbol{K}_{\boldsymbol{T}} = {}_{e}\boldsymbol{B}^{\boldsymbol{T}}\boldsymbol{C}_{\boldsymbol{elastic}}\,{}_{e}\boldsymbol{B}\,{}_{e}V\left(1 + \sum_{j=1}^{N}\gamma_j A_j\right) \tag{7.27}$$

In Equation 7.27, γ represents the coefficients of the normalized relaxation function of Prony Series that we calculate from our experimental data. Turning back to Equation 7.25, $\boldsymbol{F}_{\boldsymbol{hist}}^{n+1}$ is obtained from the element load history vectors at time step $n+1$ via assembly

$$\boldsymbol{F}_{\boldsymbol{hist}}^{n+1} = \mathrm{A}_{e=1}^{Ne}({}_{e}\boldsymbol{F}_{\boldsymbol{hist}}^{n+1}) \tag{7.28}$$

where

$${}_{e}\boldsymbol{F}_{\boldsymbol{hist}}^{n+1} = {}_{e}\boldsymbol{H}^{n+1} - {}_{e}\boldsymbol{K}_{\boldsymbol{hist}}\,{}_{e}\boldsymbol{U}^{n} \tag{7.29}$$

In Equation 7.29, ${}_{e}\boldsymbol{H}^{n+1}$ is the element history matrix at time step $n+1$, and formulated as

$${}_{e}\boldsymbol{H}^{n+1} = {}_{e}V\,{}_{e}\boldsymbol{B}^{\boldsymbol{T}}\sum_{j=1}^{N} e^{-\frac{\Delta t}{\tau_j}}\,{}_{e}\boldsymbol{h}_{\boldsymbol{j}}^{\boldsymbol{n}} \tag{7.30}$$

where ${}_e\boldsymbol{h}_j^{n+1}$ for each element can be derived from Equations 7.6 and 7.18 as

$$ {}_e\boldsymbol{h}_j^{n+1} = e^{-\frac{\Delta t}{\tau_j}} {}_e\boldsymbol{h}_j^{n} + \gamma_j A_j \boldsymbol{C}_{elastic}\, {}_e\boldsymbol{B}\left({}_e\boldsymbol{U}^{n+1} - {}_e\boldsymbol{U}^{n} \right) \tag{7.31} $$

${}_e\boldsymbol{U}^{n+1}$ and ${}_e\boldsymbol{U}^{n}$ represent nodal element displacements for the current and previous time steps respectively.

Going back to Equation 7.29, ${}_e\boldsymbol{K}_{hist}$ is the history stiffness matrix of each element and formulated as

$$ {}_e\boldsymbol{K}_{hist} = {}_e\boldsymbol{B}^{T} \boldsymbol{C}_{elastic}\, {}_e\boldsymbol{B}\, {}_eV \sum_{j=1}^{N} \gamma_j A_j \tag{7.32} $$

The numerical scheme for solving a linear viscoelastic FEM-based model is oulined in Figure 7.1. A similar, but slighly different scheme has been published by Rivkin and Givoli [63]. Given an external load, the pseudo code solves for the nodal displacements.

7.4 Integration of tissue properties into viscoelastic FEM model

Using the estimated coefficients of Prony series, we calculated the relaxation time constants, τ_j, and the normalized values of relaxation shear moduli, γ_j, by the following formula

$$ \gamma_j = \frac{E_j}{E_\infty} = \frac{G_j}{G_\infty} \tag{7.33} $$

Calculated constants were integrated into our numerical computations using the Equations 7.20 and 7.27.

A. Initializations

A.I. Given :

Δt

A.II. Given, for $j = 1, ..., N$:

γ_j *and* τ_j

A.III. Given, for $n = 0, ..., T_{end}$:

$\boldsymbol{F}_{ext}^{n}$

A.IV. Zero, for $e = 1, ..., N_e$ *and* $j = 1, ..., N$:

${}_e\boldsymbol{h}_j^0 \leftarrow \boldsymbol{0}$

B. Pre - calculations

B.I.Form, for $j = 1, ..., N$:

$$A_j = \frac{1 - e^{-\frac{\Delta t}{\tau_j}}}{\frac{\Delta t}{\tau_j}}$$

B.II.Form, for $e = 1, ..., N_e$:

$${}_e\boldsymbol{K}_{\boldsymbol{T}} = {}_e\boldsymbol{B}^{\boldsymbol{T}}\boldsymbol{C}_{elastic\ e}\boldsymbol{B}_e V\left(1 + \sum_{j=1}^{N}\gamma_j A_j\right)$$

$${}_e\boldsymbol{K}_{hist} = {}_e\boldsymbol{B}^{\boldsymbol{T}}\boldsymbol{C}_{elastic\ e}\boldsymbol{B}_e V\sum_{j=1}^{N}\gamma_j A_j$$

B.III.Assemble :

$$\boldsymbol{K}_{\boldsymbol{T}} = \mathrm{A}_{e=1}^{Ne}({}_e\boldsymbol{K}_{\boldsymbol{T}})$$

B.IV.Take inverse :

$$\boldsymbol{K}_{\boldsymbol{T}}^{-1} = I(\boldsymbol{K}_{\boldsymbol{T}})$$

B.V.Solve :

$$\boldsymbol{U}^0 = \boldsymbol{K}_{\boldsymbol{T}}^{-1}\boldsymbol{F}_{ext}^{0}$$

B.VI.Disassemble, for $e = 1, ..., N_e$:

$${}_e\boldsymbol{U}^{\boldsymbol{0}} = \mathrm{A}^{-1}(\boldsymbol{U}^{\boldsymbol{0}})$$

C. Time - step loop calculations

$n = 0, ..., T_{end} - 1$

****

C.I.Calculate, for $e = 1, ..., N_e$:

$${}_e\boldsymbol{H}^{\boldsymbol{n+1}} = {}_eV\,{}_e\boldsymbol{B}^{\boldsymbol{T}}\sum_{j=1}^{N} e^{-\frac{\Delta t}{\tau_j}}\,{}_e\boldsymbol{h}_j^{\boldsymbol{n}}$$

$${}_e\boldsymbol{F}_{\boldsymbol{hist}}^{\boldsymbol{n+1}} = {}_e\boldsymbol{H}^{\boldsymbol{n+1}} - {}_e\boldsymbol{K}_{\boldsymbol{hist}\,e}\boldsymbol{U}^{\boldsymbol{n}}$$

C.II.Assemble :

$$\boldsymbol{F}_{\boldsymbol{hist}}^{\boldsymbol{n+1}} = \mathrm{A}_{e=1}^{Ne}({}_e\boldsymbol{F}_{\boldsymbol{hist}}^{\boldsymbol{n+1}})$$

C.III.Solve :

$$\boldsymbol{U}^{\boldsymbol{n+1}} = \boldsymbol{K}_{\boldsymbol{T}}^{-1}\left[\boldsymbol{F}_{ext}^{\boldsymbol{n+1}} - \boldsymbol{F}_{\boldsymbol{hist}}^{\boldsymbol{n+1}}\right]$$

C.IV.Disassemble, for $e = 1, ..., N_e$:

$${}_e\boldsymbol{U}^{\boldsymbol{n+1}} = \mathrm{A}^{-1}(\boldsymbol{U}^{\boldsymbol{n+1}})$$

C.V.Calculate, for $e = 1, ..., N_e$ *and* $j = 1, ..., N$:

$${}_e\boldsymbol{h}_j^{\boldsymbol{n+1}} = e^{-\frac{\Delta t}{\tau_j}}\,{}_e\boldsymbol{h}_j^{\boldsymbol{n}} + \gamma_j A_j\boldsymbol{C}_{elastic\ e}\boldsymbol{B}\left({}_e\boldsymbol{U}^{\boldsymbol{n+1}} - {}_e\boldsymbol{U}^{\boldsymbol{n}}\right)$$

****

Next n

Figure 7.1: Pseudo code for solving linear viscoelastic FEM model

7.5 Implementation Details

7.5.1 Simulation environment

Our system simulates real-time behavior of a linear viscoelastic object with visual and haptic feedback to a user. The hardware components of the system include a computer monitor to display visual interactions between a linear viscoelastic deformable object and a virtual pointer, and a force-feedback device (PHANToM Model 1.0 A from SensAble Technologies) for simulating haptic interactions. We used 3D volumetric tetrahedral mesh for graphical representation of the object. The tetrahedral mesh model was developed using Tetgen 1.3.2 [64]. The underlying deformation code was written in MS Visual C++ environment, the graphical rendering of the object and the visual deformations were displayed using Open Inventor (a scene graph API), and the haptic feedback to the user was provided via PHANToM haptic device using GHOST v.4.0 driver.

7.5.2 Haptic rendering

The direct implementation of the pseudo-code given in Figure 7.1 is computationally expensive and not suitable for real-time haptic simulation. In haptic rendering of static FEM deformations using a point-based haptic rendering method, the forces displayed to the user can be calculated using the Hooke's law: $\boldsymbol{f} = \boldsymbol{kx}$, where $\boldsymbol{x}$ is the depth of penetration of the haptic interface point (HIP) into the object and $\boldsymbol{k}$ is a spring constant. Then, nodal displacements can be calculated in real-time using the FEM equation ($\boldsymbol{U} = \boldsymbol{K}^{-1}\boldsymbol{F}$) assuming that the inverse of the stiffness matrix is stored in advance. In simulation of viscoelastic deformations, one has to take into account the past loading history ("memory") of the nodes which in turn affects their displacement response. This significantly increases the number of real-time computations. In particular, the number of computations in the time-step loop (see section C in Figure 7.1) is a bottleneck for haptic rendering. For example, given Δt = 1 msec and an external force applied for 1 second, the pseudo-code in Box 1 executes the computation of nodal displacements of a 3D cube consisting of N_v = 51 vertices, N_{dof} = 153 degrees of

freedom, and N_e = 136 tetrahedrons, in approximately 1.8 seconds on a Pentium IV 2.4GHz dual-processor personal computer. For a relatively finer model, consisting of N_v = 380 vertices, N_{dof} = 1140 degrees of freedom, and N_e = 1659 tetrahedrons, the same computation takes 40 seconds. One can easily observe that sections C.II. and C.III. introduce expensive matrix calculations to the algorithm. In section C.II, there is an assembly operation executed for N_e elements. In section C.III, there is a complex multiplication of a N_{dof} x N_{dof} sparse matrix with a N_{dof} x 1 dense vector, and that complexity is directly proportional to the number of vertices in the mesh. Overall, all of these calculations are executed at each time step and the number of computations are in the order of O(N_e N^2_{dof}). Hence, the number of computations increases significantly as the degree of freedom of the model increases.

7.5.3 Real-time simulation using pre-recorded displacement and force response

In order to calculate the nodal displacements and interaction forces in real-time, we take advantage of the linearity and the superposition principle. Before the real-time simulations, we pre-record the response of each surface node to a unit step force and a unit step displacement separately. During the real-time interactions, we scale the pre-recorded forces to calculate reaction forces and superimpose the pre-recorded displacements to calculate the nodal displacements. While the pre-computation has been suggested and implemented for real-time simulation of static FEM in the past [3, 46], the application of this approach to a viscoelastic FEM is not straightforward since the displacement and force responses are time dependent. Compared to a static FEM model, the penetrations occurred in the past have to be considered for the proper calculation of future displacements and interaction forces. This time-dependent behavior is important for displaying the viscoelastic nature of the soft tissue. In our simulations, for example, the user feels the relaxation behavior of the 3D model via the forces reflected from the haptic device when he/she penetrates into the virtual object with a haptic probe and stays at certain depth for a while. The user can also visually observe the recovery behavior of the 3D model when the applied penetration is removed.

As we discuss below, the pre-computation for linear viscoelasticity is a highly involved process and the real-time computation of nodal displacements and interaction forces is quite time consuming

due the “memory” effect. At this stage, we can calculate the displacement and force response of each node to an applied load at an update rate of 100Hz using the pre-recorded data while we run the haptic loop at 1KHz. Between two consecutive time steps of the displacement and force calculations, we feed PHANToM with the force value calculated in the previous time step.

7.5.3.1 Pre-recording phase

We first find the neighbors of each surface node within a Radius of Influence (ROI). If an external force is applied to a surface node, we only consider its effect on the displacement and force calculations of nodes within ROI. For each node in ROI, we compute and record two sets of data. The first data set stores the “force-response” of a node to a unit step displacement as well as the “displacement-response” of its neighbors within ROI. The second data set stores the “recovery-displacements” of a node and its neighbors within ROI for 30 seconds when a unit step force is applied for 10 msec. When the user applies a displacement to a node or holds the node at a constant displacement during the real-time interaction, we use the first data set in tandem with the second data set for the computation of nodal displacements and the reaction forces. When the user releases the node, we use the second data set for calculating and displaying the nodal relaxations.

To construct the first data set, we conduct *stress-relaxation* experiments using our viscoelastic model. In a typical stress-relaxation experiment conducted with a tissue sample, a step displacement is applied to the sample and the relaxation of force is recorded until a steady state value is obtained. In our computations, we used the force relaxation data obtained from the real experiments performed on pig liver. The experimental force-relaxation data was recorded for 30 seconds. When the experimental force-relaxation data is applied to a particular node of the model, it returns constant nodal displacements at that node and the neighboring nodes within ROI. In our approach, the experimental force-relaxation data is scaled such that the constant nodal displacement at the node where the force is applied is 1 mm. The scaled force-relaxation data is recorded as the “force-response” and the resulting nodal displacements within ROI are recorded as the “displacement-response” of the node.

To construct the second data set, we conduct *creep* experiments using the same viscoelastic model. We apply a unit force for 10 msec to a node and then record the computed "recovery-displacements" of that node and its neighboring nodes within ROI for 30 seconds. We observed that this time duration is more than sufficient for nodal displacements to reach steady state values. Figure 7.2 presents the recovery effect in response to a unit force applied to a node for 10 seconds. To display the creep and relaxation behavior more clearly, the force is applied to Node 13 for 10 sec instead of 10 msec.

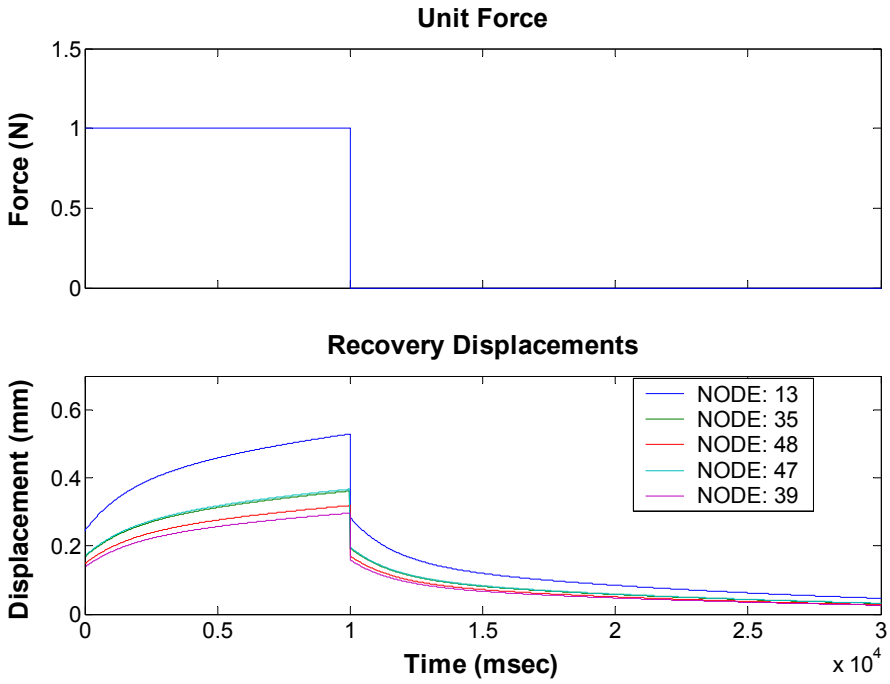

Figure 7.2: A unit force is applied to node 13 for 10 seconds (top). The resultant "recovery-displacements" of the nodes within ROI are displayed (bottom). The largest displacement is naturally observed at node 13.

7.5.3.2 Real-time Computation Phase

During the real-time interactions, we first check for the collisions between HIP and the undeformed state of the object. If HIP is outside the undeformed state of the object, there is no collision and no force is displayed to the user. If HIP is inside, there may or may not be a collision depending on the *displacement histories* of the nodes. The recovery effect of penetrations occurred in the past add up to create, what we call, the displacement history of the nodes (see Figure 7.3). Our database returns object's closest surface node to HIP as the contacted node and the depth of penetration into the undeformed state of the object. The current displacement of the contacted node retrieved from the displacement history is compared with the penetration depth of HIP. If the amount of penetration is less than the current displacement of the contacted node, there is no collision and no force is displayed to the user. If not, there is a collision and the penetration amount is calculated as the difference between the penetration of HIP into the undeformed object and the current displacement of the contacted node.

If a collision is detected, we first compute the reaction forces to be displayed to the user via a haptic device by scaling the "force-response" data of the contacted node by the penetration amount. The "displacement-response" of the contacted node is also scaled by the penetration amount and superimposed to the displacement history of the nodes in ROI to calculate their current displacement. We, then calculate the effect of the current penetration to the displacement history. For this purpose, we have created a C++ class with members named as *time of activation*, *contact node id*, and *scale factor*. If a penetration occurs, we immediately create an instance of this class and set the time of activation to the current time, contact node id to index of the contacted node and the scale factor to the force value displayed to the user. This instance is then added to a list of instances created up to the current time. To calculate the displacement history of a node at a particular time, all instances in the list are examined and their "recovery-displacements" are scaled by the scale factor of each instance and added to each other (see Figure 7.3). Since we assume that recovery-displacement data of a particular node converge to a constant value after 30 sec, we delete the instances older than 30 sec from the list, and use the converged value instead. Therefore, there can be a maximum of 3000 instances at any time for an update rate of 100Hz.

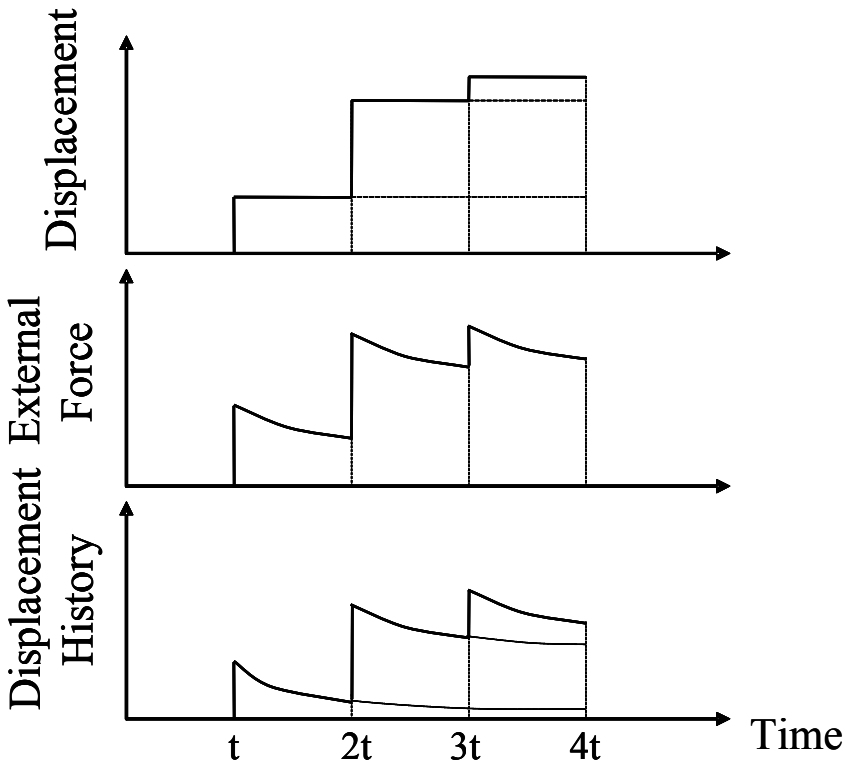

Figure 7.3: Force (middle) response is computed based on displacement input (top). Recovery effects of past and present penetrations are scaled based on calculated force and superimposed to generate displacement history (bottom).

7.6 Validation

For validation of our viscoelastic FEM model and the pre-computation approach, we performed experiments with a 3D cube consisting of $N_v = 51$ vertices, $N_{dof} = 153$ degrees of freedom, and $N_e = 136$ tetrahedrons. The displacements of the nodes at the bottom surface of the cube were constrained in the vertical y-direction. In order to validate our linear viscoelastic FEM, we have conducted two sets of *compression* tests with the 3D cube. We also conducted the same tests on the 3D cube using ANSYS FEM package. In the first compression test, we applied 1.0 N to all nodes of the top surface

for 30 seconds. The resultant displacement responses of our viscoelastic FEM and the ANSYS model are shown in Figure 7.4. In the second compression test, we applied 1 mm displacement to the same nodes on the top surface for 30 seconds using ANSYS. Then, we used the force relaxation data obtained from ANSYS model in our viscoelastic model to calculate the displacement response of the same nodes (see Figure 7.5). The results of both compression tests conducted with our viscoelastic model perfectly match with the results of ANSYS.

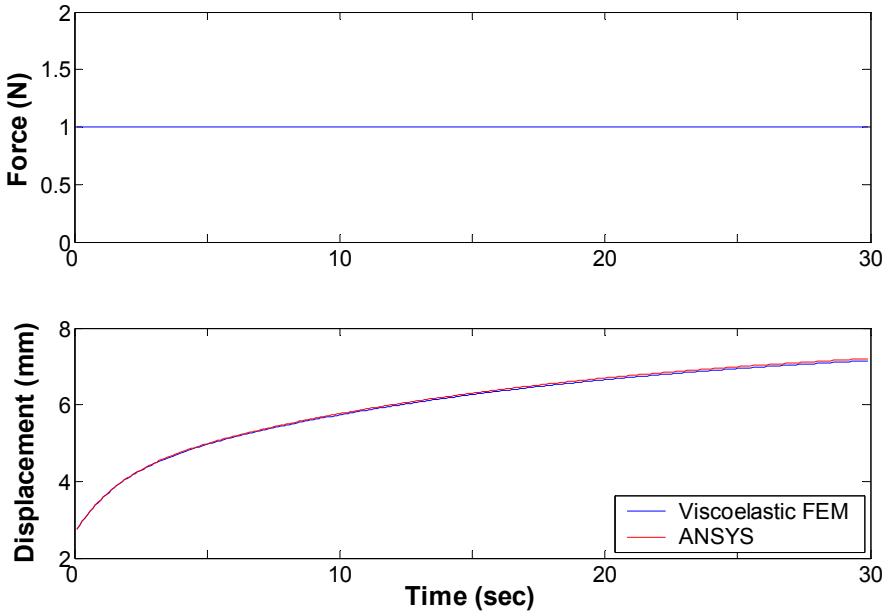

Figure 7.4: The first compression test: Using ANSYS, the cube was compressed by applying 1.0 N to all nodes of the FEM model on the top surface (top). The displacement response of node 13 was calculated using our viscoelastic FEM model and ANSYS model (bottom).

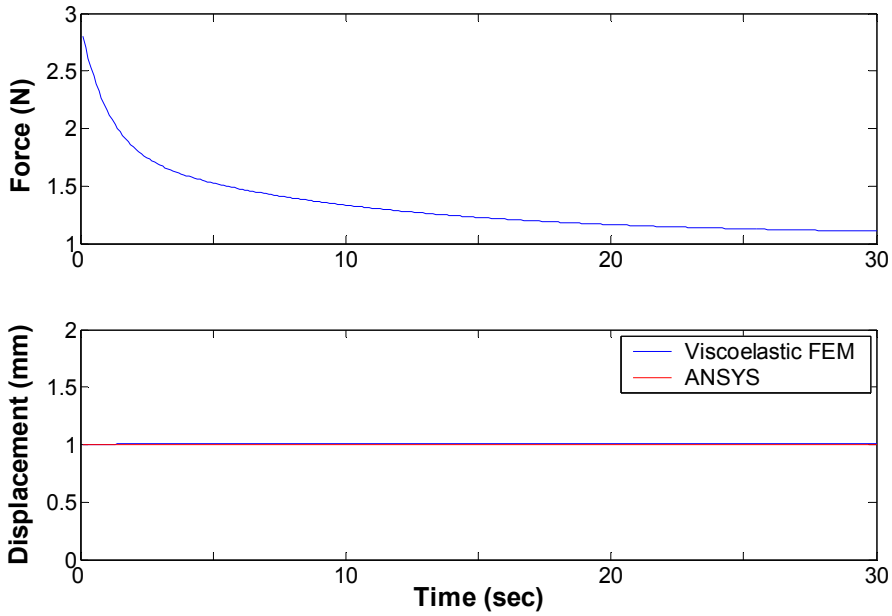

Figure 7.5: The second compression test: Using ANSYS, the cube was compressed by applying 1.0 mm to all nodes of the FEM model on the top surface (bottom). The force response of the nodes (top) was recorded and then entered to our viscoelastic FEM to compute their displacement response (bottom).

After showing that our viscoelastic model is correct and works accurately, a real-time test with the haptic device was performed to validate the proposed superposition approach. In this test, first the middle node (Node 13) at the top surface was indented to a certain depth by the haptic device and held there for a while. Then, it was released and one of the neighboring nodes was indented. The nodal displacements and external forces acting on all nodes were recorded (see Figure 7.6.a and 7.6.b). In order to compare our superposition approach with the actual linear viscoelastic model, external forces recorded during the real-time interaction were supplied to our viscoelastic model and nodal displacements were obtained. As it is shown in Figure 7.6.d, the error between the displacement values calculated through superposition approach and ones calculated through the linear viscoelastic model is in the order of one hundreds of a millimeter for nodal displacements of a few millimeters.

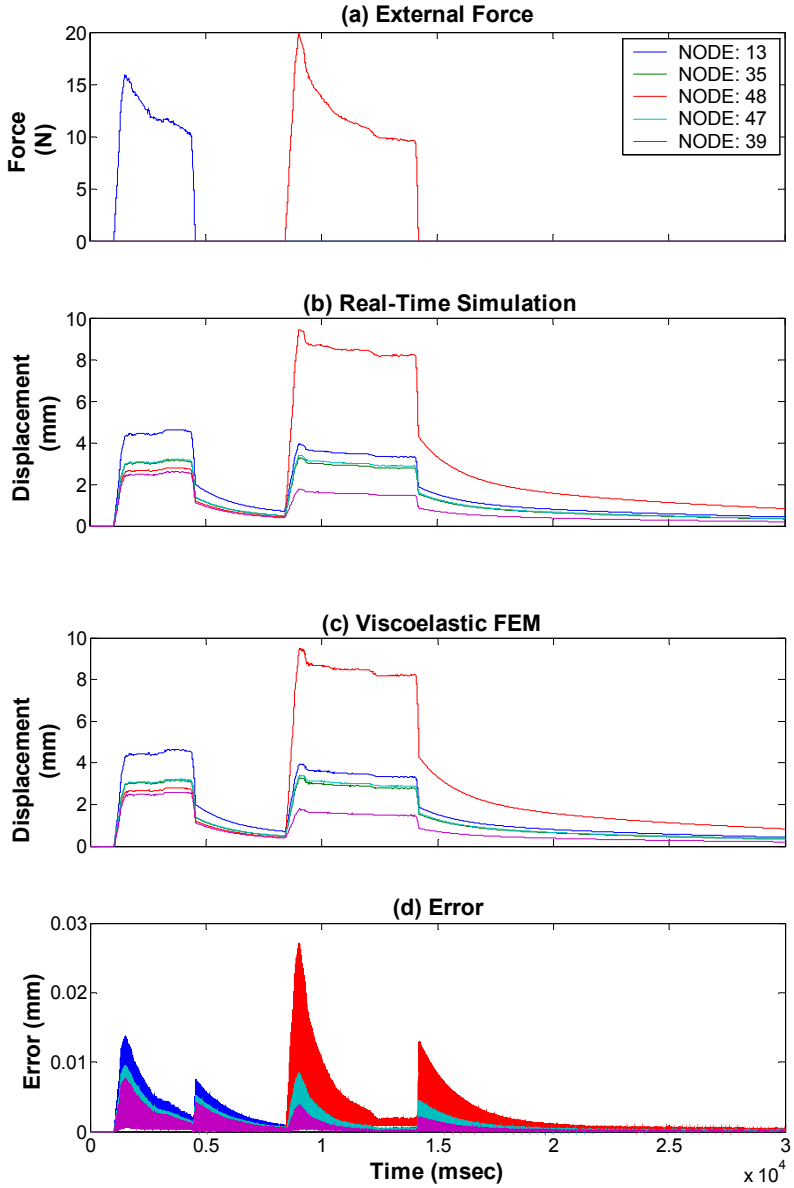

Figure 7.6: The real-time validation test. Using the haptic device, node 13 and node 48 were indented sequentially in real-time **(b)**. The external forces calculated using the superposition approach **(a)** were entered to the actual linear viscoelastic model to calculate nodal displacements **(c)**. The error is the difference between the displacement values calculated through superposition approach and the ones calculated through actual linear viscoelastic model **(d)**.

7.7 Discussion

There are limited number of studies on real-time viscoelastic simulation of tissue behavior using FEM [35, 55]. Since viscoelastic materials are significantly influenced by the rate of loading, the past displacement and force history of each node in the model play an important role in the behavior of the model and have to be stored and updated at each time step. In this chapter, a new linear viscoelastic FEM formulation derived from a generalized Maxwell model has been presented. We have integrated the real experimental data collected laparascopically from a pig liver into our model. We have also proposed a superposition approach for the real-time execution of the linear viscoelastic model. While the superposition approach has been applied to real-time static FEM simulation in the past, to our knowledge, it has not been extended to real-time linear viscoelastic simulation yet. For this purpose, we conducted stress-relaxation and creep experiments in virtual domain using the developed linear viscoelastic FEM. We recorded the force and displacement response of each surface node of a 3D cube to a unit step displacement and a unit step force respectively. During the real-time interactions with the 3D cube, the resultant force and displacement responses of the nodes were calculated by scaling the pre-recorded force and superimposing the displacement data. The developed model and proposed superposition approach have been validated using ANSYS. In the current implementation of the superposition approach, we pre-calculate and record the "displacement-response", "force-response", and the "recovery-displacements" of each surface node in the form of individual data points. This consumes significant storage space in memory. In the future, we plan to employ curve fitting to the recorded force and displacement data and store the data as a set of coefficients rather than individual data points.

Chapter 8

CONCLUSIONS AND FUTURE WORK

8.1 Conclusions

An inverse finite element solution for soft tissue characterization and a new numerical scheme for real-time simulation of soft organs are presented in this thesis. We have designed a robotic indenter for the minimally invasive measurement of *in-situ* material properties of soft tissues during a laparoscopic surgery. Using the indenter, animal experiments were conducted and force-displacement and force-time responses of pig liver were successfully measured under static and dynamic loading conditions. In this thesis, we present the results of our *in-situ* experiments conducted with three pigs. The material properties of pig liver were determined in three steps. First, using the elastic contact model with small deformation assumption (i.e. the Lee and Radok's solution [58]), the effective Young's modulus of the liver was estimated as around 10-15 kPa from the force-displacement data of static indentations. A supporting value of 10-15 kPa was obtained by Ottensmeyer [13]. Then, the time-dependent force relaxation function was represented by 2-term Prony series to estimate viscoelastic material properties. The coefficients of Prony series were estimated from the data of stress relaxation experiments via curve fitting. We observed that relaxation curves of pig liver for different initial loadings almost overlap with each other which is an indication of linear viscoelastic response. As a final step, the viscoelastic and nonlinear hyperelastic material properties were determined using an inverse finite element solution through iterations. To construct the finite element model of the liver, homogeneous, isotropic, nonlinear (hyperelastic), time-dependent (viscoelastic) and nearly incompressible material properties were assumed. Geometry of the organ around the contact region was simplified to a 2D axisymmetric square. Hyperelastic behavior of the liver was modeled using Mooney-Rivlin strain-energy function and viscoelastic behavior was modeled using

Prony series having two-terms. The estimated effective elastic modulus and the viscoelastic coefficients obtained through the curve fitting process were used as initial values in the optimization. The estimated coefficients of Prony series by the inverse finite element solution are slightly different than the values obtained by curve fitting. The difference due to the step input assumption and invalidity of the Lee and Radok's solution [58] at large indentations. Using the estimated hyperelastic and viscoelastic parameters, the static indentation experiments were conducted in ANSYS. The experimental force displacement response of pig liver does not perfectly match with the numerical ANSYS solution, but the numerical solution is in the range of experimental data.

The estimated viscoelastic tissue properties were then integrated into a 3D linear viscoelastic finite element model for real-time simulation. We have proposed a new pre-computation method based on superposition principle for real-time computation of nodal displacements and interaction forces. While the superposition approach has been applied to real-time static FEM simulation in the past, to our knowledge, it has not been extended to real-time linear viscoelastic simulation yet. To implement the superposition approach, we performed stress-relaxation and creep using the developed linear viscoelastic FEM and a 3D cube. We recorded the force and displacement response of each surface node of the 3D cube to a unit step displacement and a unit step force respectively. During the real-time interactions with the 3D cube, the resultant force and displacement responses of the nodes were calculated by scaling the pre-recorded force data and by superimposing the displacement data respectively. The developed model and the proposed pre-computation approach have been both validated using ANSYS.

8.2 Future Work

While the number of studies on *in-vivo* measurement of animal organ properties is increasing, there are only a few studies available in the literature on humans [11, 12]. Both of these groups performed human experiments during an open surgery using hand-held probes though they used different techniques to collect data. Our measurement system was designed by considering the issues of sterilization, safety, and minimally invasive surgery (MIS) compatibility since we plan to conduct human experiments in the future. Although we successfully performed animal experiments, there are

still some problems to be solved in order to perform human experiments. During the experiments some leakage of carbon dioxide gas was observed through the holes of the indenter as the indenter was inserted through one of the trocars. The holes were covered by a surgical tape and leakage was stopped during our measurements. This problem must be solved before human experiments. In addition, the stress relaxation experiments require long term loading of soft tissue that lasts for several seconds. It is obvious that long-term loading is not possible in human experiments since assisted ventilation can be used for only short period of time. As an alternative solution, oscillatory loading can be applied to organ to investigate viscoelastic material properties [21]. For this purpose, we conducted sinusoidal indentation experiments with 3 pigs and measured the force response at 8 different frequencies. During the analysis of data, we observed that the inertia of the robot arm excessively affects the measurements at high frequencies. As a future work, we plan to characterize the dynamics of the robotic arm to remove the inertial effects from the experimental data. Then, the relaxation function can be characterized in frequency domain.

In this thesis, we have also proposed a numerical scheme and an efficient superposition approach for real-time simulation of viscoelastic tissue behavior. In the current implementation of the superposition approach, we pre-calculate and record the “displacement-response”, “force-response”, and the “recovery-displacements” of each surface node in the form of individual data points. This consumes significant storage space in memory. In the future, we plan to employ curve fitting to the recorded force and displacement data and store it as a set of coefficients rather than individual data points.

BIBLIOGRAPHY

[1] Basdogan, C., De, S., Kim, J., Muniyandi, M., Srinivasan, M.A., "Haptics in Minimally Invasive Surgical Simulation and Training", IEEE Computer Graphics and Applications, Vol. 24, No.2, (2004), pp. 56-64.

[2] Basdogan, C., Ho, C, and Srinivasan, M.A., "Virtual Environments for Medical Training: Graphical and Haptic Simulation of Common Bile Duct Exploration," IEEE-ASME Trans. Mechatronics, Vol. 6, No. 3, (2001), pp. 267-285.

[3] Cotin, S., Delingette, H., Ayache, N., "Real-time elastic deformations of soft tissues for surgery simulation", Visualization and Computer Graphics, IEEE Transactions, Vol. 5, Issue 1, (1999), pp. 62 – 73

[4] Kuhnapfel, U.G., Krumm, H.G., Kuhn, C., Hubner, M., Neisius, B., "Endosurgery simulations with KISMET: A flexible tool for surgical instrument design, operation room planning and VR technology based abdominal surgery training", In: Proc. Virtual Reality World'95. Stuttgart, (1995), pp. 165–171.

[5] Bro-Nielsen, M., Helfrick, D., Glass, B., Zeng, X., Connacher, H., "VR simulation of abdominal trauma surgery", In: Proc. MMVR'98. IOS Press, (1998), pp. 117–123. X.

[6] Szekély, G., Brechbühler, C., Dual, J., Enzler, R., Hug, J., Haller, U., Hutter, R., Ironmonger, N., Kauer, M., Meier, V., Neiderer, P., Rhomberg, A., Schmid, P., Schweitzer, G., Thaler, M., Vuskovic, V., and Tröster, G., Haller, U., Bajka, M., "Virtual reality-based simulation of endoscopic surgery", Prescence 9, 3 (2000), 313.333.

[7] Székely G. et al., "Modeling of Soft Tissue Deformation for Laparoscopic Surgery Simulation," Proc. 1st Int'l Conf. Medical Image Computing and Computer-Assisted Intervention (MICCAI), LNCS 1496, Springer-Verlag, (1998), pp. 550-561.

[8] Fung Y.C. Biomechanics: Mechanical properties of living tissues. 2nd ed. Springer-Verlag, New York, (1993).

[9] Ottensmeyer M.P., Kerdok A.E., Howe R.D, Dawson S.L., "The Effects of Testing Environment on the Viscoelastic Properties of Soft Tissues", Proc. of International Symposium on Medical Simulation (2004), pp. 9-18, Cambridge, MA.

[10] Brown J.D., Rosen J., Kim Y.S., Chang L., Sinanan M.N., Hannaford B., "In-vivo and In-Situ Compressive Properties of Porcine Abdominal Soft Tissues", MMVR, Vol. 94, Newport Beach, CA (2003), pp. 26-32.

[11] Kauer M., "Inverse finite element characterization of soft tissues with aspiration experiments", Ph.D. Thesis, Institute of Mechanical Systems (2001), Diss No: 14233, ETH.

[12] Carter F.J., Frank T.G., Davies P.J., McLean D., Cuschieir A., "Measurements and modeling of the compliance of human and porcine organs", Medical Image Analysis, Vol. 5 (2001), pp 231-236.

[13] Ottensmeyer M. P., "Minimally Invasive Instrument for In vivo Measurement of Solid Organ Mechanical Impedance", Ph.D. Thesis, Dept. of Mechanical Engineering (2001), MIT.

[14] Tay B. K., Stylopoulos N., De S., Rattner D. W., Srinivisan M. A., "Measurement of In-vivo Force Response of Intra-Abdominal Soft Tissues for Surgical Simulation", Proc. MMVR Conference (2002), pp 514-519.

[15] Gefen A., Margulies S.S., "Are in vivo and in situ brain tissues mechanically similar?", Journal of Biomechanics, Vol. 37 (2004), 1339-1352.

[16] Miller K. and Chinzei K., "Modeling of Brain Tissue Mechanical Properties. Bi-phasic versus Single-phase Approach", in Proc. 3rd Intl. Symp. Comp. Methods in Biomech & Biomed Eng (1997)

[17] Nasseri S., Bilston L. E., Phan-Thien N., "Viscoelastic Properties of Pig Kidney in Shear, Experimental Results and Modeling", Rheol Acta, Vol. 41 (2002), pp 180-192.

[18] Brouwer I., Ustin J., Bentley L., Sherman A., Dhruv N., and Tendick F., "Measuring In Vivo Animal Soft Tissue Properties for Haptic Modeling in Surgical Simulation", Proc. MMVR Conference (2001), pp 69-71.

[19] Maaß H., Kühnapfel U., "Noninvasive Measurement of Elastic Properties of Living Tissues", in Proc. of CARS (1999).

[20] Kim J., "Virtual Environments for Medical Training: Graphical and Haptic Simulation of Tool-tissue Interactions", Ph.D. Thesis, Dept. of Mechanical Engineering (2003), MIT, Cambridge.

[21] Findley W. N., Lai J.S., Onaran K,. Creep and Relaxation of Nonlinear Viscoelastic Materials, Dover, New York, (1976).

[22] Shaw, S., Whiteman, J. R.,. "Robust Adaptive Finite Element Schemes for Viscoelastic Solid Deformation: An Investigative Study", Final report for the US Army's European Research Office Seed Project, (1999).

[23] Macioce, P., "Viscoelastic Damping 101". http://www.roushind.com/news_downloads/white_papers/SV_Damping101.pdf

[24] Nash M., "Mechanics and Material Properties of the Heart using an Anatomically Accurate Mathematical Model", Ph.D. Thesis, Department of Engineering Science, The University of Auckland New Zealand (1998).

[25] Johansson T., Meier P, and Blickhan R, "A finite-element Model for the Mechanical Analysis of Skeletal Muscles", J theor. Biol., vol. 206, (2000), pp 131-149

[26] Centers for Disease Control and Prevention. Sterilization or Disinfection of Medical Devices: General Principles. http://www.cdc.gov/ncidod/hip/sterile/sterile.htm

[27] Basdogan C., Srinivasan M.A., "Haptic Rendering In Virtual Environments", Handbook of Virtual Environments, Ed: K. Stanney, (2002), pp. 117-134.

[28] Graham, R., PID Controller Tunning Notes, http://www.tcnj.edu/~rgraham/PID-tuning.html.

[29] Kauer M., Vuskovic V., Dual J., Szekely G. and Bajka M., "Inverse finite element characterization of soft tissues", Medical Image Analysis, Vol. 6 (2002), pp 275-287.

[30] Tönük E., and Silver-Thorn M. B., "Nonlinear Elastic Material Property Estimetion of Lower Extremity Residual Limb Tissue", IEEE Transactions on Neural Systems and Rehabilitation Engineering, Vol. 11 (2003), pp 43-53.

[31] Han L., Noble J.A., and Burcher M., "A Novel Ultrasound Indentation System For Measuring Biomechanical Properties of *In Vivo* Soft Tissue", Ultrasound in Med. & Biol., Vol. 29 (2003), pp 813-823.

[32] Liu Y., Kerdok A.E., and Howe R.D., "A Nonlinear Finite Element Model of Soft Tissue Indentation", Proc. of ISMS 2004, Vol. 3078 (2004), pp 67-76.

[33] Samani A., and Plewes D., "A method to measure the hyperelastic parameters of *ex vivo* breast tissue samples", Phys. Med. Biol., Vol. 49 (2004), pp 4395-4405.

[34] Schnur D.S., and Zabaras N., “An Inverse Method for Determining Elastic Material Properties and a Material Interface”, International Journal for Numerical Methods in Engineering, Vol. 33 (1991), pp 2039-2057.

[35] Hauth, M., GroB, J., StraBer, W., “Interactive Physically Based Solid Dynamics”, Eurographics/SIGGRAPH Symposium on Computer Animation (2003), pp 17-27.

[36] Mazzella, K.M.F., Latombe, J., “The forcegrid: A buffer structure for haptic interaction with virtual elastic objects”, Proc. of IEEE International Conference on Robotics and Automation (2002), pp 939-946.

[37] James, D.L., Pai, D.K., “ArtDefo - Accurate Real Time Deformable Objects”, Proc. of SIGGRAPH (1999), pp. 65–72.

[38] Delingette, H., Cotin, S., Ayache, N., “A hybrid elastic model allowing real-time cutting, deformations and force-feedback for surgery training and simulation”, Proc. of Computer Animation (1999), pp. 70 – 81.

[39] Kim, J., De, S., Srinivasan, M.A., “An Integral Equation Based Multiresolution Modeling Scheme for Multimodal Medical Simulations”, Proceedings of the 11th Symposium on Haptic Interfaces for Virtual Environment and Teleoperator Systems (2003), p.221

[40] Kuhnapfel, U.G., Krumm, H.G., Kuhn, C., Hubner, M., Neisius, B., “Endosurgery simulations with KISMET: A flexible tool for surgical instrument design, operation room planning and VR technology based abdominal surgery training”, In: Proc. Virtual Reality World (1995), pp. 165–171.

[41] Cover, S.A., Ezquerra, N.F., O’Brien, J.F., Rowe, R., Gadacz, T., Palm, E., “Interactively deformable models for surgery simulation”, IEEE Computer Graphics & Applications (1993), pp. 68-75.

[42] Lee, Y., Terzopoulos, D., Waters, K., “Realistic modeling for facial animation”, In Proc. SIGGRAPH’95, Los Angeles, CA, August, (1995), pp. 55–62.

[43] DiMaio, S.P., Salcudean, S.E., “Interactive simulation of needle insertion models”, Biomedical Engineering, IEEE Transactions on Volume 52, Issue 7 (2005), pp. 1167 – 1179.

[44] DiMaio, S.P., Salcudean, S.E., “Needle insertion modeling and simulation” Robotics and Automation, IEEE Transactions on Volume 19, Issue 5 (2003), pp. 864 – 875.

[45] Gibson, S.F.F, Mirtich, B., “A Survey of Deformable Modeling in Computer Graphics”, MERL Technical Report, TR97-19 (1997).

[46] Basdogan, C., "Real-time Simulation of Dynamically Deformable Finite Element Models Using Modal Analysis and Spectral Lanczos Decomposition Methods", Proceedings of the Medicine Meets Virtual Reality Conference (2001).

[47] Gibson, S., Fyock, C., Grimson, E., Kanade, T., Kikinis, R., Lauer, H., McKenzie, N., Mor, A., Nakajima, S., Ohkami, H., Osborne, R., Samosky, J., Sawada, A., "Volumetric Object Modeling for Surgical Simulation", Medical Image Analysis, Vol. 2, No. 2 (1998), pp. 121-132.

[48] Cotin, S., Delingette, H., “Real-time surgery simulation with haptic feedback using finite elements”, Proc. of IEEE International Conference on Robotics and Automation, Vol. 4 (1998), pp. 3739 – 3744.

[49] Wu, X., Downes, M. S., Goktekin, T., Tendick, F., “Adaptive nonlinear finite elements for deformable body simulation using dynamic progressive meshes”, Proc. of Comp. Graphics Forum, Vol. 20(3) (2001), pages 349–358.

[50] Picinbono, G., Delingette, H., and Ayache , N., “Non-linear and anisotropic elastic soft tissue models for medical simulation”, ICRA (2001).

[51] Tsap, L., Goldgof, D., and Sarkar, S., “Efficient nonlinear finite element modeling of nonrigid objects via optimization of mesh models”, Journal of Computer Vision and Image Understanding, Vol. 69(3) (1998), pp. 330–350

[52] Müller, M., Dorsey, J., McMillan, L., Jagnov, R., Cutler, B., "Stable Real-Time Deformations", Proceedings of the 2002 ACM SIGGRAPH/Eurographics symposium on Computer animation, (2002).

[53] Bro-Nielsen, M., Cotin, S., “Real-time volumetric deformable models for surgery simulation using finite elements and condensation”, Computer Graphics Forum, Vol. 15(3) (1996), pp. 57-66.

[54] Delingette, H., Ayache, N., “Soft Tissue Modeling for Surgery Simulation”, Handbook of Numerical Analysis, Vol. 12 (2004), pp. 453-550.

[55] Schoner J.L., Lang J, Seidel H.-P., “Measurement-Based Interactive Simulation of Viscoelastic Solids”, Proceedings of the Eurographics, Vol. 23, No. 3 (2004).

[56] Debunne, G., Desbrun, M., Cani, M.P., Barr, A.H., "Dynamic real-time deformations using space & time adaptive sampling", Proceedings of SIGGRAPH (2001), pp. 31.36.

[57] Haddad, Y.M., Viscoelasticity of Engineering Materials. Chapman & Hall, London, (1995).

[58] Lee, E.H., Radok, J.R.M., "The contact problem for viscoelastic bodies", Journal of Applied Mechanics, Vol. 27 (1960), pp. 438–444.

[59] ANSYS, Inc. Basic Structural Nonlinearities. Training Manual for Release 5.6 (2000)

[60] ANSYS, Inc. Release 8.1 Documentation (2004)

[61] Kaliske, M., Rothert, H., "Formulation and implementation of three-dimensional viscoelasticity at small and finite strains", Computational Mechanics, Vol. 19 (1997), pp. 228-239.

[62] Zienkiewicz, O., Taylor, R., (2000). The finite element method, Vol. 1-3. Oxford: Butterworth-Heinemann.

[63] Rivkin, L., Givoli, D., "An efficient finite element scheme for viscoelasticity with moving boundaries", Computational Mechanics, Vol. 24 (2000), pp. 503-512.

[64] Si, H., (2004). "Tetgen: A Quality Tetrahedral Mesh Generator and Three-Dimensional Delaunay Triangulator"

[65] Felippa C. A., (2001). Nonlinear Finite Element Methods. Department of Aerospace Engineering Sciences and Center for Space Structures and Controls.

[66] Lakes R., Viscoelastic Solids. CRC Press, (1998).

[67] Weiss J. A., Maker B. N., Govindjee S., "Finite element implementation of incompressible, transversely isotropic hyperelasticty", Comput. Methods Appl. Mech. Eng., Vol. 135 (1996), pp. 107-128.

[68] SensAble Technologies, Phantom premium haptic device, Model 1.0 http://www.sensable.com/products/phantom_ghost/phantom.asp

[69] ATI Industrial Automation, Nano 17 force-torque transducer, http://www.ati-ia.com/products/ft/sensors.aspx

[70] National Instruments, Analog input card, NI PCI-6034 http://sine.ni.com/nips/cds/view/p/lang/en/nid/11916